CrossMark

KEPLER-1647B: THE LARGEST AND LONGEST-PERIOD *KEPLER* TRANSITING CIRCUMBINARY PLANET

Veselin B. Kostov[1,25], Jerome A. Orosz[2], William F. Welsh[2], Laurance R. Doyle[3], Daniel C. Fabrycky[4],
Nader Haghighipour[5], Billy Quarles[6,7,25], Donald R. Short[2], William D. Cochran[8], Michael Endl[8], Eric B. Ford[9],
Joao Gregorio[10], Tobias C. Hinse[11,12], Howard Isaacson[13], Jon M. Jenkins[14], Eric L. N. Jensen[15], Stephen Kane[16],
Ilya Kull[17], David W. Latham[18], Jack J. Lissauer[14], Geoffrey W. Marcy[13], Tsevi Mazeh[17], Tobias W. A. Müller[19],
Joshua Pepper[20], Samuel N. Quinn[21,26], Darin Ragozzine[22], Avi Shporer[23,27], Jason H. Steffen[24], Guillermo Torres[18],
Gur Windmiller[2], and William J. Borucki[14]

[1] NASA Goddard Space Flight Center, Mail Code 665, Greenbelt, MD 20771, USA; veselin.b.kostov@nasa.gov
[2] Department of Astronomy, San Diego State University, 5500 Campanile Drive, San Diego, CA 92182, USA
[3] SETI Institute, 189 Bernardo Avenue, Mountain View, CA 94043; and Principia College, IMoP, One Maybeck Place, Elsah, IL 62028, USA
[4] Department of Astronomy and Astrophysics, University of Chicago, 5640 South Ellis Avenue, Chicago, IL 60637, USA
[5] Institute for Astronomy, University of Hawaii-Manoa, Honolulu, HI 96822, USA
[6] Department of Physics and Physical Science, The University of Nebraska at Kearney, Kearney, NE 68849, USA
[7] NASA Ames Research Center, Space Science Division MS 245-3, Code *SST*, Moffett Field, CA 94035, USA
[8] McDonald Observatory, The University of Texas as Austin, Austin, TX 78712-0259, USA
[9] Department of Astronomy and Astrophysics, The Pennsylvania State University, 428A Davey Lab, University Park, PA 16802, USA
[10] Atalaia Group and Crow-Observatory, Portalegre, Portugal
[11] Korea Astronomy and Space Science Institute (KASI), Advanced Astronomy and Space Science Division, Daejeon 305-348, Korea
[12] Armagh Observatory, College Hill, BT61 9DG Armagh, Northern Ireland, UK
[13] Department of Astronomy, University of California Berkeley, 501 Campbell Hall, Berkeley, CA 94720, USA
[14] NASA Ames Research Center, Moffett Field, CA 94035, USA
[15] Department of Physics and Astronomy, Swarthmore College, Swarthmore, PA 19081, USA
[16] Department of Physics and Astronomy, San Francisco State University, 1600 Holloway Avenue, San Francisco, CA 94132, USA
[17] Department of Astronomy and Astrophysics, Tel Aviv University, 69978 Tel Aviv, Israel
[18] Harvard-Smithsonian Center for Astrophysics, 60 Garden Street, Cambridge, MA 02138, USA
[19] Institute for Astronomy and Astrophysics, University of Tuebingen, Auf der Morgenstelle 10, D-72076 Tuebingen, Germany
[20] Department of Physics, Lehigh University, Bethlehem, PA 18015, USA
[21] Department of Physics and Astronomy, Georgia State University, 25 Park Place NE Suite 600, Atlanta, GA 30303, USA
[22] Department of Physics and Space Sciences, Florida Institute of Technology, 150 W. University Boulevard, Melbourne, FL 32901, USA
[23] Jet Propulsion Laboratory, California Institute of Technology, 4800 Oak Grove Drive, Pasadena, CA 91109, USA
[24] Department of Physics and Astronomy, Northwestern University, 2145 Sheridan Road, Evanston, IL 60208, USA

ABSTRACT

We report the discovery of a new *Kepler* transiting circumbinary planet (CBP). This latest addition to the still-small family of CBPs defies the current trend of known short-period planets orbiting near the stability limit of binary stars. Unlike the previous discoveries, the planet revolving around the eclipsing binary system Kepler-1647 has a very long orbital period (~1100 days) and was at conjunction only twice during the *Kepler* mission lifetime. Due to the singular configuration of the system, Kepler-1647b is not only the longest-period transiting CBP at the time of writing, but also one of the longest-period transiting planets. With a radius of $1.06 \pm 0.01\ R_{\rm Jup}$, it is also the largest CBP to date. The planet produced three transits in the light curve of Kepler-1647 (one of them during an eclipse, creating a syzygy) and measurably perturbed the times of the stellar eclipses, allowing us to measure its mass, $1.52 \pm 0.65\ M_{\rm Jup}$. The planet revolves around an 11-day period eclipsing binary consisting of two solar-mass stars on a slightly inclined, mildly eccentric ($e_{\rm bin} = 0.16$), spin-synchronized orbit. Despite having an orbital period three times longer than Earth's, Kepler-1647b is in the conservative habitable zone of the binary star throughout its orbit.

Key words: binaries: eclipsing – planetary systems – stars: individual (KIC-5473556, Kepler-1647) – techniques: photometric

1. INTRODUCTION

Planets with more than one sun have long captivated our collective imagination, yet direct evidence of their existence has emerged only in the past few years. Eclipsing binaries (EBs), in particular, have long been thought of as ideal targets to search for such planets (Borucki & Summers 1984; Schneider & Chevreton 1990; Schneider & Doyle 1995; Jenkins et al. 1996; Deeg et al. 1998). Early efforts to detect transits of a circumbinary planet (CP) around the EB system CM Draconis—a particularly well suited system composed of two M dwarfs on a nearly edge-on orbit—suffered from incomplete temporal coverage (Schneider & Doyle 1995; Doyle et al. 2000; Doyle & Deeg 2004). Several nontransiting circumbinary candidates have been proposed since 2003, based on measured timing variations in binary stellar systems (e.g., Zorotovic & Schreiber 2013). The true nature of these candidates remains, however, uncertain, and rigorous dynamical analysis has challenged the stability of some of the proposed systems (e.g., Hinse et al. 2014; Horner et al. 2011, 2012; Schleicher et al. 2015). It was not until 2011 and the continuous monitoring of thousands of EBs provided by

NASA's *Kepler* mission that the first CP, Kepler-16b, was unambiguously detected through its transits (Doyle et al. 2011). Today, data from the mission have allowed us to confirm the existence of 10 transiting CPs in eight EB systems (Doyle et al. 2011; Orosz et al. 2012a, 2012b, 2015, in preparation; Welsh et al. 2012, 2015; Kostov et al. 2013, 2014; Schwamb et al. 2013). Curiously enough, these planets have all been found to orbit EBs from the long-period part of the *Kepler* EB distribution and have orbits near the critical orbital separation for dynamical stability (Welsh et al. 2014; Martin et al. 2015).

These exciting new discoveries provide better understanding of the formation and evolution of planets in multiple stellar systems and deliver key observational tests for theoretical predictions (e.g., Paardekooper et al. 2012; Marzari et al. 2013; Pelupessy & Portegies Zwart 2013; Rafikov 2013; Kley & Haghighipou 2014, 2015; Bromley & Kenyon 2015; Chavez et al. 2015; Lines et al. 2015; Miranda & Lai 2015; Silsbee & Rafikov 2015). Specifically, numerical simulations indicate that CBPs should be common, typically smaller than Jupiter, and close to the critical limit for dynamical stability—due to orbital migration of the planet toward the edge of the precursor disk cavity surrounding the binary star (Pierens & Nelson 2007, 2008, 2013, hereafter PN07, PN08, PN15). Additionally, the planets should be coplanar (within a few degrees) for binary stars with sub-AU separation due to disk–binary alignment on precession timescales (Foucart & Lai 2013, 2014). The orbital separation of each new CBP discovery, for example, constrains the models of protoplanetary disks and migration history and allows us to discern between an observational bias and a migration pileup (Kley & Haghighipou 2014, 2015). Discoveries of misaligned transiting CBPs such as Kepler-413b (Kostov et al. 2014) and Kepler-453b (Welsh et al. 2015) help determine the occurrence frequency of CBPs by arguing for the inclusion of a distribution of possible planetary inclinations into abundance estimates (Schneider 1994; Armstrong et al. 2014; Kostov et al. 2014; Martin & Triaud 2014).

In terms of stellar astrophysics, the transiting CBPs provide excellent measurements of the sizes and masses of their stellar hosts and can notably contribute toward addressing a known tension between the predicted and observed characteristics of low-mass stars, where the stellar models predict smaller (and hotter) stars than observed (Torres et al. 2010; Boyajian et al. 2012; but also see Tal-Or et al. 2013). Each additional CBP discovery sheds new light on the still-uncertain mechanism for the formation of close binary systems (Tohline 2002). For example, the lack of CBPs around a short-period binary star (period less than ~7 days) lends additional support for a commonly favored binary formation scenario of a distant stellar companion driving tidal friction and Kozai–Lidov circularization of the initially wide host binary star toward its current close configuration (Kozai 1962; Lidov 1962; Mazeh & Shaham 1979; Fabrycky & Tremaine 2007; Hamers et al. 2015; Martin et al. 2015; Muñoz & Lai 2015).

Here we present the discovery of the Jupiter-size transiting CBP Kepler-1647b, which orbits its 11.2588-day host EB every ~1100 days—the longest-period transiting CBP at the time of writing. The planet completed a single revolution around its binary host during *Kepler*'s data collection and was at inferior conjunction only twice—at the very beginning of the mission (Quarter 1) and again at the end of Quarter 13. The planet transited the secondary star during the same conjunction and both the primary and secondary stars during the second conjunction.

The first transit of the CBP Kepler-1647b was identified and reported in Welsh et al. (2012); the target was subsequently scheduled for short-cadence (SC) observations as a transiting CBP candidate (Quarters 13 through 17). At the time, however, this single event was not sufficient to rule out contamination from a background star or confirm the nature of the signal as a transit of a CBP. As *Kepler* continued observing, the CBP produced a second transit—with duration and depth notably different from the first transit—suggesting a planet on an orbit of either ~550 days or ~1100 days. The degeneracy stemmed from a gap in the data where a planet on the former orbit could have transited (e.g., Armstrong et al. 2014; Welsh et al. 2014). After careful visual inspection of the *Kepler* light curve, we discovered another transit, heavily blended with a primary stellar eclipse a few days before the second transit across the secondary star. As discussed below, the detection of this blended transit allowed us to constrain the period and pin down the orbital configuration of the CBP—both analytically and numerically.

This paper is organized as follows. We describe our analysis of the *Kepler* data (Section 2) and present our photometric and spectroscopic observations of the target (Section 3). Section 4 details our analytical and photometric-dynamical characterization of the CB system and outlines the orbital dynamics and long-term stability of the planet. We summarize and discuss our results in Section 5 and draw conclusions in Section 6.

2. *Kepler* DATA

Kepler-1647 is listed in the NExScI Exoplanet Archive as a 11.2588-day period EB with a *Kepler* magnitude of 13.545. It has an estimated effective temperature of 6217 K, surface gravity log$g$ of 4.052, metallicity of −0.78, and primary radius of 1.464 $R_\odot$. The target is classified as a detached EB in the *Kepler* EB Catalog, with a morphology parameter $c = 0.21$ (Prša et al. 2011; Slawson et al. 2011; Matijevič et al. 2012; Kirk et al. 2015). The light curve of Kepler-1647 exhibits well-defined primary and secondary stellar eclipses with depths of ~20% and ~17%, respectively, separated by 0.5526 in phase (see *Kepler* EB Catalog). A section of the raw (SAPFLUX) *Kepler* light curve of the target, containing the prominent stellar eclipses and the first CBP transit, is shown in the top panel of Figure 1.

2.1. Stellar Eclipses

The information contained in the light curve of Kepler-1647 allowed us to measure the orbital period of the EB and obtain the timing of the stellar eclipse centers (T_{prim}, T_{sec}), the flux and radius ratio between the two stars (F_B/F_A and R_B/R_A), the inclination of the binary (i_{bin}), and the normalized stellar semimajor axes (R_A/a_{bin}, R_B/a_{bin}) as follows.[28] First, we extracted subsections of the light curve containing the stellar eclipses and the planetary transits. We only kept data points with quality flags less than 16 (see *Kepler* user manual)—the rest were removed prior to our analysis. Next, we clipped out each eclipse, fit a fifth-order Legendre polynomial to the out-of-eclipse section only, and then restored the eclipse and

---

[28] Throughout this paper we refer to the binary with a subscript "bin," to the primary and secondary stars with subscripts "A" and "B," respectively, and to the CBP with a subscript "p."
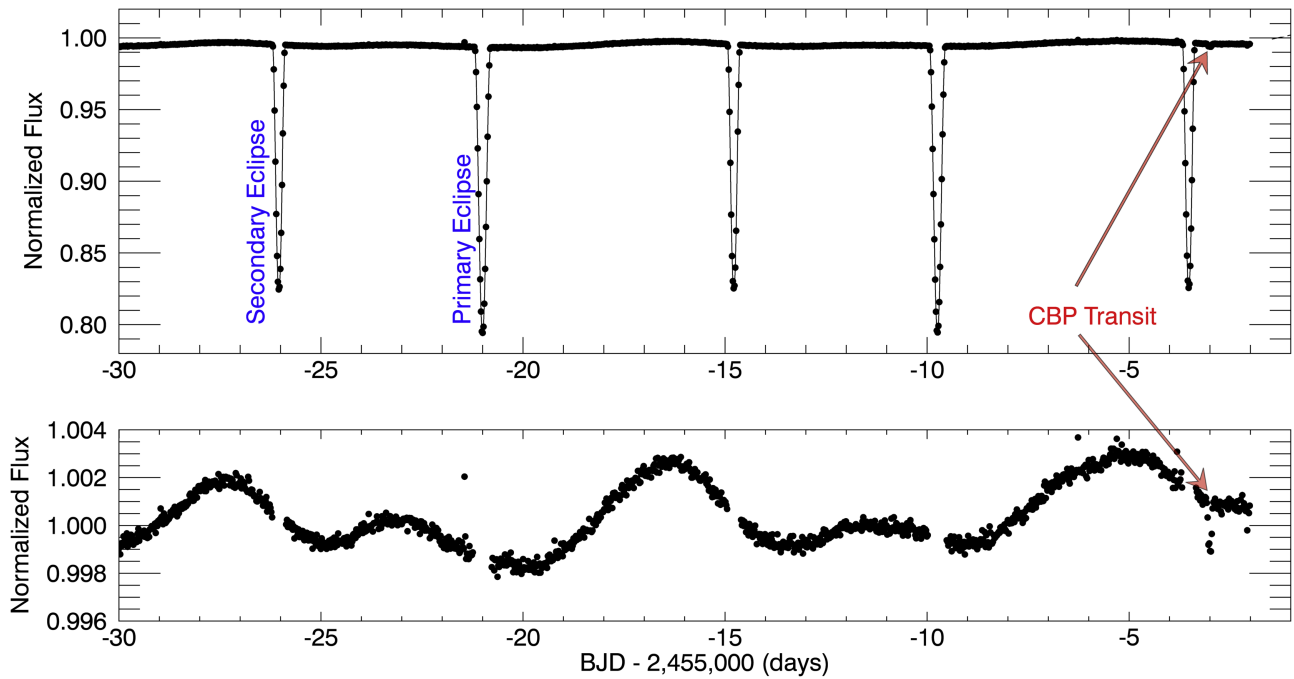
Figure 1. Top panel: representative section of the raw (SAPFLUX), LC light curve of Kepler-1647 (black symbols) exhibiting two primary stellar eclipses, three secondary stellar eclipses, and the first transit of the CBP. Bottom panel: same, but with the stellar eclipses removed and zoomed in to show the ~11-day out-of eclipse modulation. This represents the end of Quarter 1, which is followed by a few-days-long data gap. Note the differences in scale between the two panels.

normalized to unity. Finally, we modeled the detrended, normalized, and phase-folded light curve using the eclipsing light curve (ELC) code (Orosz & Hauschildt 2000; Welsh et al. 2015). A representative sample of SC primary and secondary stellar eclipses, along with our best-fit model and the respective residuals, is shown in Figure 2.

To measure the individual mid-eclipse times, we first created an eclipse template by fitting a Mandel & Agol (2002) model to the phase-folded light curve for both the primary and secondary stellar eclipses. We carefully chose five primary and secondary eclipses (see Figure 2) where the contamination from spot activity—discussed below—is minimal. Next, we slid the template across the light curve, iteratively fitting it to each eclipse by adjusting only the center time of the template while keeping the EB period constant. We note that the SC eclipse models were binned to obtain long-cadence (LC) models, which were used to estimate the eclipse times over the entire data set. The results of the SC and LC data analysis were merged, with preference given to the SC data.

We further used the measured primary and secondary eclipse times to calculate eclipse time variations (ETVs). These are defined in terms of the deviations of the center times of each eclipse from a linear ephemeris fit through all primary and all secondary mid-eclipse times, respectively (for a common binary period).

The respective primary and secondary "Common Period Observed minus Calculated" (CPOC, or O−C for short) measurements are shown in Figure 3. The 1σ uncertainty is ~0.1 minutes for the measured primary eclipses and ~0.14 minutes for the measured secondary eclipses. As seen from the figure, the divergence in the CPOC is significantly larger than the uncertainties.

The measured CPOC is a key ingredient in estimating the mass of the CBP. As in the case of Kepler-16b, Kepler-34b, and Kepler-35b (Doyle et al. 2011; Welsh et al. 2012), the

gravitational perturbation of Kepler-1647b imprints a detectable signature on the measured ETVs of the host EB— indicated by the divergent primary (black symbols) and secondary (red symbols) CPOCs shown in Figure 3. We note that there is no detectable "chopping" in the ETVs (Deck & Agol 2015) and, given that the CBP completed a single revolution during the observations, interpreting its effect on the ETVs is not trivial. However, the divergence in the CPOC residuals cannot be fully explained by a combination of general relativity (GR) correction[29] and classical tidal apsidal motion. The former is the dominant effect, with analytic $\Delta\omega_{GR} = 0.00019$ deg/cycle, while the latter has an analytic contribution of $\Delta\omega_{tidal} = 0.00003$ deg/cycle (using the best-fit apsidal constants of $k_2(A) = 0.00249$ for the slightly evolved primary and $k_2(B) = 0.02978$ for the secondary).

The total analytic precession rate, $\Delta\omega_{analytic} = \Delta\omega_{GR} + \Delta\omega_{tidal} = 0.00022$ deg/cycle, is ≈9.5% smaller than the numeric rate of $\Delta\omega_{numeric} = 0.00024$ (deg/cycle), as calculated from our photodynamical model (Section 4). The difference represents the additional push from the CBP to the binary's apsidal motion and allowed us to evaluate the planet's mass. Thus, the relative contributions to the apsidal precession of the binary star are $\Delta\omega_{GR} = 77.4\%$, $\Delta\omega_{tidal} = 13.9\%$, and $\Delta\omega_{CBP} = 8.7\%$. The difference between the analytic and numerically determined precession rates is significant—for a test-mass planet the latter agrees with the former to within 0.5%.

Following the method of Welsh et al. (2015), we also analyzed the effect of starspots on the measured eclipse times by comparing the local slope of the light curve outside the stellar eclipses to the measured ETVs (see also Orosz et al. 2012b; Holczer et al. 2015; Mazeh et al. 2015). While

---

[29] The GR contribution is fixed for the respective masses, period, and eccentricity of the binary star.
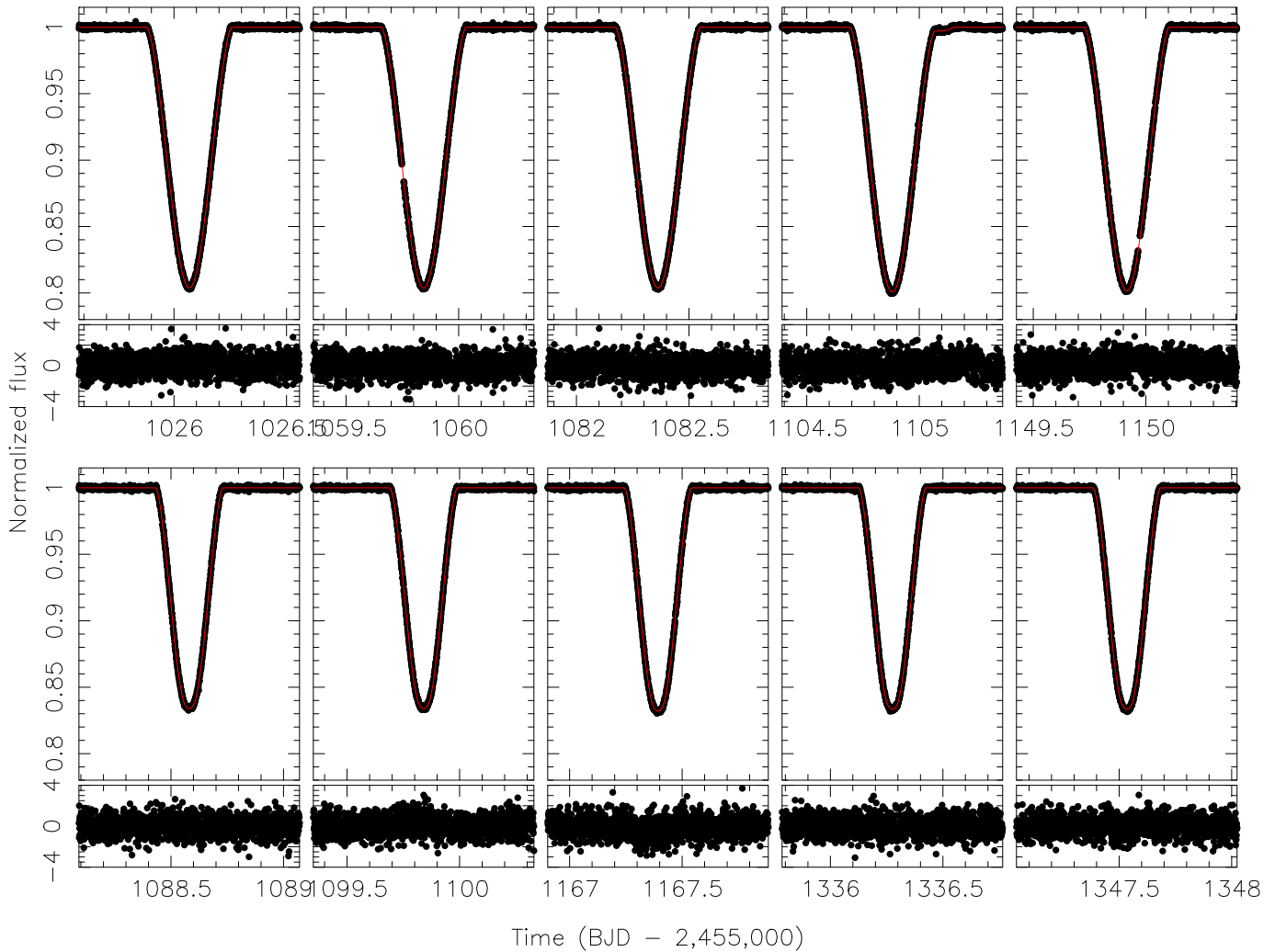
Figure 2. Representative sample of primary (top row) and secondary (bottom row) stellar eclipses in SC data along with our best-fit model (red) and the respective residuals. The black symbols represent normalized SC flux as a function of time (BJD–2,455,000). A blended transit of the CBP can be seen during primary stellar eclipse near day 1105 (top row, fourth panel from the left; the model includes the planetary transit).

there is no apparent correlation for the primary eclipse ETVs (Figure 4, left panel), we found a clear, negative correlation for the secondary eclipses (Figure 4, right panel), indicating that the observed light-curve modulations are due to the rotationally modulated signature of starspots moving across the disk of the secondary star. The negative correlation also indicates that the spin and orbital axes of the secondary star are well aligned (Holczer et al. 2015; Mazeh et al. 2015). We have corrected the secondary eclipse times for this anticorrelation. We note that as the light from the secondary is diluted by the primary star, its intrinsic photometric modulations are larger than the observed 0.1%–0.3%, indicating a rather active secondary star. The power spectra of the O−C ETVs (in terms of measured primary and secondary eclipse times minus linear ephemeris) are shown in Figure 5. There are no statistically significant features in the power spectrum.

The exquisite quality of the *Kepler* data also allowed for precise measurement of the photometric centroid position of the target. Apparent shifts in this position indicate either a contamination from nearby sources (if the centroid shifts away from the target during an eclipse or transit) or that the source of the studied signal is not the *Kepler* target itself (if the shift is toward the target during an eclipse or transit, see Conroy et al.

2014). As expected, Kepler-1647 exhibits a clear photocenter shift away from the target and toward the nearby star during the eclipses, indicating that the eclipses are indeed coming from the target stars, and that some light contamination from a nearby star is present in the *Kepler* aperture. We discuss this in more detail in Section 3.3.

2.2. Stellar Rotation

The out-of-eclipse sections of the light curve are dominated by quasi-periodic flux modulations with an amplitude of 0.1%–0.3% (bottom panel of Figure 1). To measure the period of these modulations, we performed both a Lomb–Scargle (L–S) and an autocorrelation function (ACF) analysis of the light curve. For the latter method, based on measuring the time lags of spot-induced ACF peaks, we followed the prescription of McQuillan et al. (2013a, 2014). Both methods show clear periodic modulations (see Figures 1 and 6), with $P_{\rm rot} = 11.23 \pm 0.01$ days—very close to the orbital period of the binary. We examined the light curve by eye and confirmed that this is indeed the true period.

To measure the period, we first removed the stellar eclipses from the light curve using a mask that was 1.5 times the
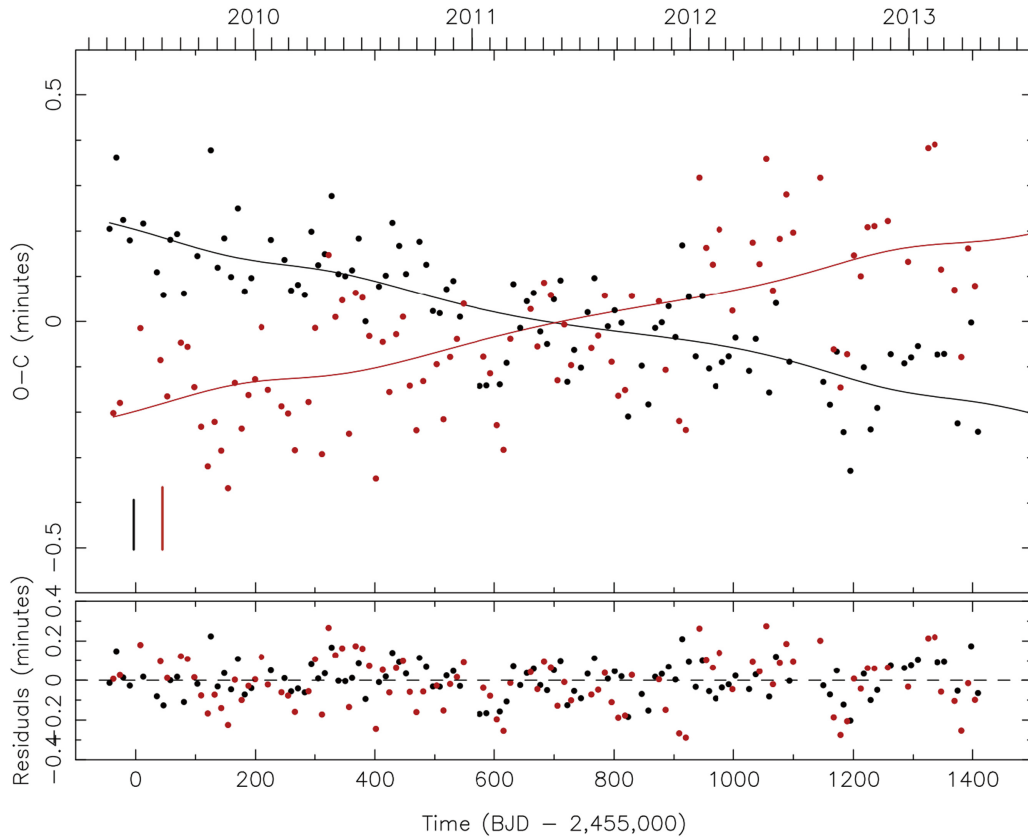
Figure 3. Top panel: measured "Common Period Observed minus Calculated" (CPOC, or O−C for short) for the primary (black symbols) and secondary (red symbols) stellar eclipses; the respective lines indicate the best-fit photodynamical model. The divergent nature of the CPOCs constrains the mass of the CBP. Bottom panel: CPOC residuals based on the photodynamical model. The respective average error bars are shown in the lower left of the top panel.

duration of the primary eclipse (0.220 days) and centered on each eclipse time. After the eclipses were removed, a seventh-order polynomial was used to moderately detrend each quarter. In Figure 6 we show the mildly detrended SAPFLUX light curve covering Q1-16 *Kepler* data (top panel), the power spectrum as a function of the logarithmic frequency (middle panel), and the ACF of the light curve (bottom panel). Each quarter shown in the top panel had a seventh-order polynomial fit divided out to normalize the light curve, and we also clipped out the monthly data-download glitches by hand, and any data with Data Quality Flag >8. The inset in the bottom panel zooms out to better show the long-term stability of the ACF; the vertical black dashed lines in the middle and bottom panels represent the best-fit orbital period of the binary star, and the red dotted lines represent the expected rotation period if the system were in pseudosynchronous rotation. The periods as derived from the ACF and from L–S agree exactly.

The near equality between the orbital and the rotation period raises the question whether the stars could be in pseudosynchronous pseudo-equilibrium. If this is the case, then with $P_{\rm bin} = 11.258818$ days and $e_{\rm bin} = 0.16$, and based on Hut's formula (Hut 1981a, 1982), the expected pseudosynchronous period is $P_{\rm pseudo,rot} = 9.75$ days. Such spin-orbit synchronization should have been reached within 1 Gyr.[30] Thus, the secondary star is not rotating pseudosynchronously. This is clearly illustrated in Figure 6, where the red dotted line in the

inset in the bottom panel represents the pseudosynchronous rotation period.

Our measurement of the near equality between $P_{\rm rot}$ and $P_{\rm bin}$ indicates that the rotation of both stars is synchronous with the binary period (due to tidal interaction with the binary orbit). Thus, the secondary (G-type) star appears to be tidally spun up since its rotation period is faster than expected for its spectral type and age (discussed in more detail in Section 5), and has driven the large stellar activity, as seen by the large-amplitude starspots. The primary star does not appear to be active. The spin-up of the primary (an F-type star) should not be significant since F stars naturally rotate faster and are quieter than G stars (assuming the same age). As a result, the primary could seem quiet compared to the secondary—but this can change as the primary star evolves. As seen from Figure 6, the starspot modulation is indeed at the binary orbital period (black dashed line, inset in bottom panel).

There is reasonable evidence that stars evolving off the main sequence look quieter than main-sequence stars (at least for a while); stars with shallower convection zones look less variable at a given rotation rate (Bastien et al. 2014). The convective zone of the primary star is probably too thin for significant spot generation at that rotation period. As we show in Section 5, the secondary star has mass and effective temperature very similar to the Sun, so it should be generating spots at about the same rate as the Sun would have done when it was at the age of NGC 6811—where early G stars have rotation periods of 10–12 days (Meibom et al. 2011).

---

[30] Orbital circularization takes orders of magnitude longer and is not expected.
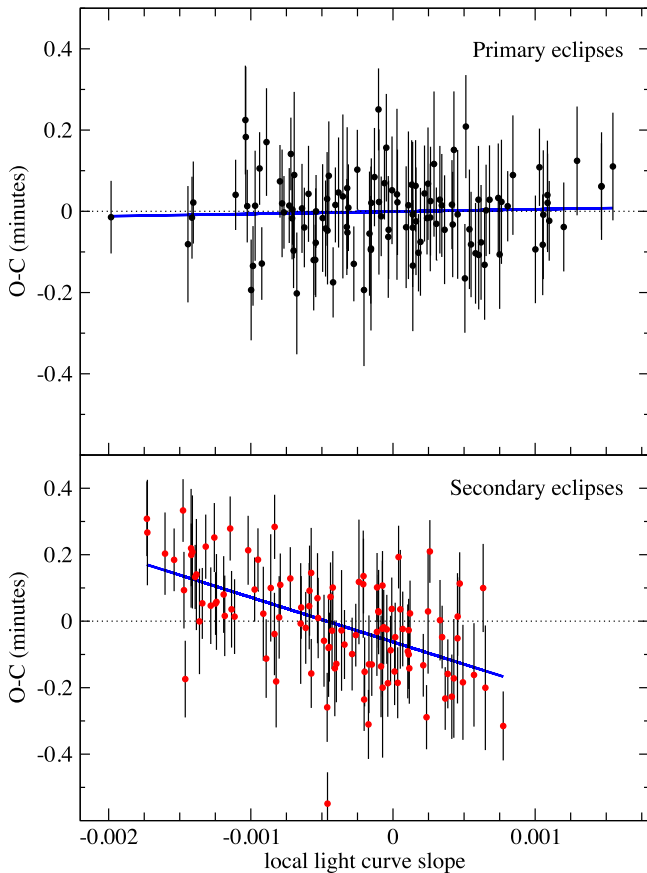
Figure 4. Measured local slope (see text for details) of the light curve during primary (top panel) and secondary (bottom panel) stellar eclipses as a function of the respective Observed minus Calculated ("O−C") eclipse times. The anticorrelation seen for the secondary eclipses indicates that the modulations seen in the light curve are caused by the rotation of the secondary star.

Based on the photodynamically calculated stellar radii R_A and R_B (Section 5) and on the measured P_{rot}, if the two stars are indeed synchronized, then their rotational velocities should be $V_{rot,A} \sin i_A = 8.04 \, \mathrm{km \, s^{-1}}$ and $V_{rot,B} \sin i_B = 4.35 \, \mathrm{km \, s^{-1}}$. If, on the contrary, the two stars are rotating pseudosynchronously, their respective velocities should be $V_{rot,A} \sin i_A = 9.25 \, \mathrm{km \, s^{-1}}$ and $V_{rot,B} \sin i_B = 5.00 \, \mathrm{km \, s^{-1}}$.

The spectroscopically measured rotational velocities (Section 3.1) are $V_{rot,A} \sin i_A = 8.4 \pm 0.5 \, \mathrm{km \, s^{-1}}$ and $V_{rot,B} \sin i_B = 5.1 \pm 1.0 \, \mathrm{km \, s^{-1}}$, respectively—assuming $5.5 \, \mathrm{km \, s^{-1}}$ macroturbulence for the primary star (Doyle et al. 2014) and $3.98 \, \mathrm{km \, s^{-1}}$ macroturbulence for solar-type stars (Gray 1984) as appropriate for the secondary. Given the uncertainty on both the measurements and the assumed macroturbulence, the measured rotational velocities are not inconsistent with synchronization.

Combined with the measured rotation period, and assuming spin-orbit synchronization of the binary, the measured broadening of the spectral lines constrains the stellar radii:

$$ R_B = \frac{P_{rot} V_{rot,B} \sin i_B}{2\pi \phi}, \tag{1} $$

where ϕ accounts for differential rotation and is a factor of order unity. Assuming $\phi = 1$, $R_B = 1.1 \pm 0.2 \, R_\odot$ and $R_A = 1.85 R_B = 2.08 \pm 0.37 \, R_\odot$.

3. SPECTROSCOPIC AND PHOTOMETRIC FOLLOW-UP OBSERVATIONS

To complement the *Kepler* data and better characterize the Kepler-1647 system, we obtained comprehensive spectroscopic and photometric follow-up observations. Here we describe the radial velocity measurements we obtained to constrain the spectroscopic orbit of the binary and calculate the stellar masses, its orbital semimajor axis, eccentricity, and argument of periastron. We also present our spectroscopic analysis constraining the effective temperature, metallicity, and surface gravity of the two stars, our direct-imaging observations aimed at estimating flux contamination due to unresolved background sources, and our ground-based observations of stellar eclipses to extend the accessible time baseline past the end of the original *Kepler* mission.

3.1. Spectroscopic Follow-up and Radial Velocities

We monitored Kepler-1647 spectroscopically with several instruments in order to measure the radial velocities of the two components of the EB. Observations were collected with the Tillinghast Reflector Echelle Spectrograph (TRES; Fűresz 2008) on the 1.5 m telescope at the Fred L. Whipple Observatory, the Tull Coude Spectrograph (Tull et al. 1995) on the McDonald Observatory 2.7 m Harlan J. Smith Telescope, the High Resolution Echelle Spectrometer (HIRES; Vogt et al. 1994) on the 10 m Keck I telescope at the W. M. Keck Observatory, and the Hamilton Echelle Spectrometer (HamSpec; Vogt 1987) on the Lick Observatory 3 m Shane telescope.

A total of 14 observations were obtained with TRES (eight in 2011, five in 2012, and one in 2013). They span the wavelength range from about 390 to 900 nm at a resolving power of $R \approx 44,000$. We extracted the spectra following the procedures outlined by Buchhave et al. (2010). Seven observations were gathered with the Tull Coude Spectrograph in 2011, each consisting of three exposures of 1200 s. This instrument covers the wavelength range 380–1000 nm at a resolving power of $R \approx 60,000$. The data were reduced and extracted with the instrument pipeline. Two observations were obtained with HIRES also in 2011, covering the range 300–1000 nm at a resolving power of $R \approx 60,000$ at 550 nm. We used the C2 decker for sky subtraction, giving a sky-projected area for the slit of $0''87 \times 14''0$. Th-Ar lamp exposures were used for wavelength calibration, and the spectra were extracted with the pipeline used for planet search programs at that facility. Finally, two spectra were collected with HamSpec in 2011, with a wavelength coverage of 385–955 nm and a resolving power of $R \approx 60,000$. The measured radial velocities are shown in Figure 7.

All of these spectra are double-lined.[31] RVs for both binary components from the TRES spectra were derived using the two-dimensional cross-correlation technique TODCOR (Zucker & Mazeh 1994), with templates taken from a library of synthetic spectra generated from model atmospheres by R. L. Kurucz (see Nordstroem et al. 1994; Latham et al. 2002). These templates were calculated by John Laird, based on a line list compiled by Jon Morse. The synthetic spectra cover

---

[31] We note that Kolbl et al. (2015) detected the spectrum of the secondary star as well and obtained its effective temperature ($T_{\rm eff,B} \sim 5900$ K) and flux ratio ($F_B/F_A = 0.22$)—fully consistent with our analysis.
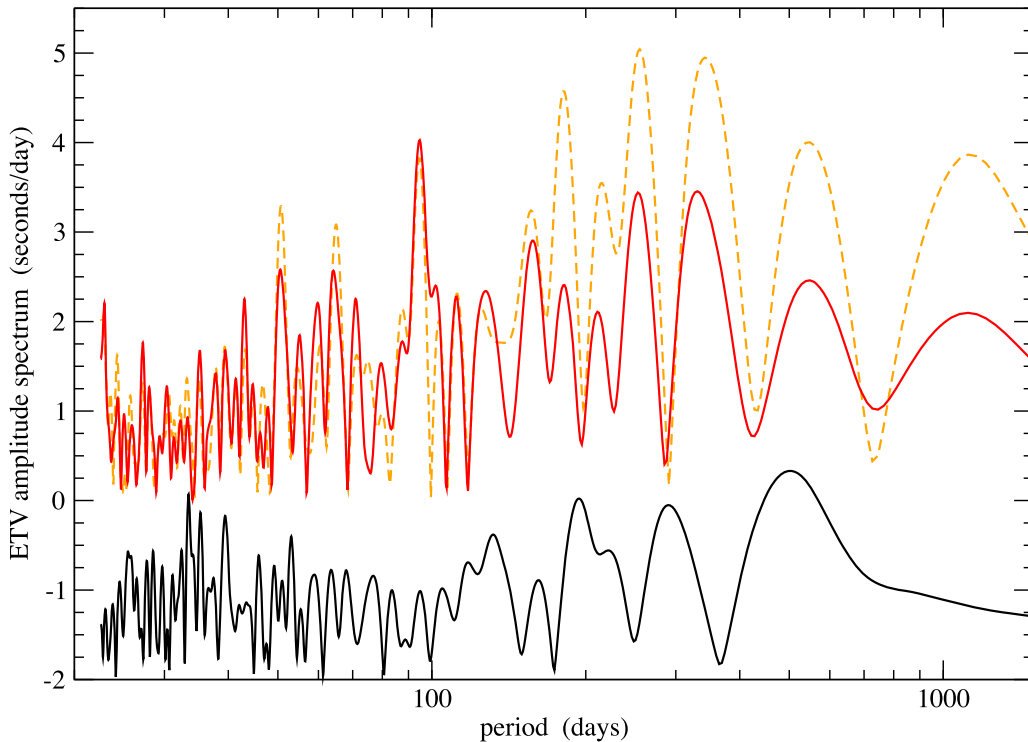
Figure 5. Power spectrum of the primary (black line) and secondary (solid red and dashed orange lines) O−C eclipse times (based on a linear ephemeris). The primary power spectrum is offset vertically for viewing purposes. The dashed orange and solid red lines represent the secondary ETV power spectrum before and after correcting for the anticorrelation between the local slope of the light curve and the measured secondary eclipse times (see Figure 4). There are no statistically significant peaks in either the primary or corrected secondary ETVs.

30 nm centered near 519 nm, though we only used the central 10 nm, corresponding to the TRES echelle order centered on the gravity-sensitive Mg I b triplet. Template parameters (effective temperature, surface gravity, metallicity, and rotational broadening) were selected as described in the next section.

To measure the RVs from the other three instruments, we used the "broadening function" (BF) technique (e.g., Schwamb et al. 2013), in which the Doppler shift can be obtained from the centroid of the peak corresponding to each component in the broadening function, and the rotational broadening is measured from the peak's width. This method requires a high-resolution template spectrum of a slowly rotating star, for which we used the RV standard star HD 182488 (a G8V star with an RV of $+21.508$ km s^{-1}; see Welsh et al. 2015). All HJDs in the Coordinated Universal Time (UTC) frame were converted to BJDs in the Terrestrial Time (TT) frame using the software tools by Eastman et al. (2010). It was also necessary to adjust the RV zero points to match that of TRES by $+0.66$ km s^{-1} for McDonald, by -0.16 km s^{-1} for Lick, and by $+0.28$ km s^{-1} for Keck. We report all radial velocity measurements in Table 1.

3.2. Spectroscopic Parameters

In order to derive the spectroscopic parameters (T_{eff}, $\log g$, [m/H], $v \sin i$) of the components of the Kepler-1647 binary, both for obtaining the final radial velocities and also for later use in comparing the physical properties of the stars with stellar evolution models, we made use of TODCOR as a convenient tool to find the best match between our synthetic spectra and the observations. Weak spectra or blended lines can prevent

accurate classifications, so we included in this analysis only the 11 strongest TRES spectra (S/N > 20), and we note that all of these spectra have a velocity separation greater than 30 km s^{-1} between the two stars.

We performed an analysis similar to the one used to characterize the stars of the CBP-hosting double-lined binaries Kepler-34 and Kepler-35 (Welsh et al. 2012), but given slight differences in the analysis that are required by the characteristics of this system, we provide further details here. We began by cross-correlating the TRES spectra against a (five-dimensional) grid of synthetic composite spectra that we described in the previous section. The grid we used for Kepler-1647 contains every combination of stellar parameters in the ranges $T_{eff,A} = [4750, 7500]$, $T_{eff,B} = [4250, 7250]$, $\log g_A = [3.0, 5.0]$, $\log g_B = [3.5, 5.0]$, and [m/H] = $[-1.0, +0.5]$, with grid spacings of 250 K in T_{eff} and 0.5 dex in $\log g$ and [m/H] (12,480 total grid points).[32] At each step in the grid, TODCOR was run in order to determine the RVs of the two stars and the light ratio that produces the best-fit set of 11 synthetic composite spectra, and we saved the resulting mean correlation peak height from these 11 correlations. Finally, we interpolated along the grid surface defined by these peak heights to arrive at the best-fit combination of stellar parameters.

This analysis would normally be limited by the degeneracy between spectroscopic parameters (i.e., a nearly equally good fit can be obtained by slightly increasing or decreasing T_{eff},

---

[32] We ran a separate TODCOR grid solely to determine the $v \sin i$ values, which we left fixed in the larger grid. This is justified because the magnitude of the covariance between $v \sin i$ and the other parameters is small. This simplification reduces computation time by almost two orders of magnitude.
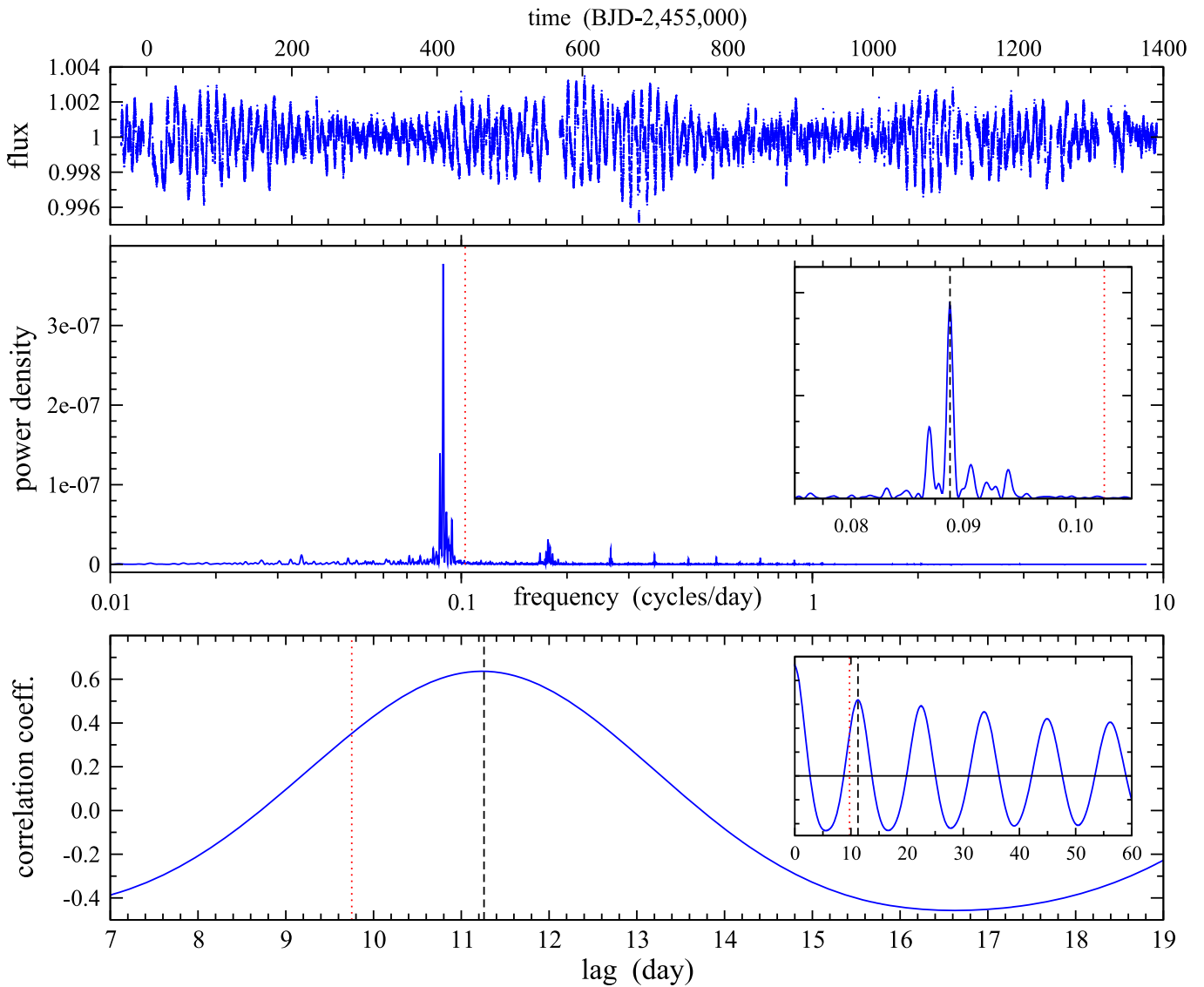
Figure 6. Top panel: mildly detrended, normalized raw (SAPFLUX) light curve for the Q1-16 *Kepler* data; middle panel: L–S periodogram of the out-of-eclipse regions of the light curve, revealing a clear peak near 11 days; bottom panel: ACF of the light curve. The inset in the middle panel is zoomed out to better represent the long-term stability of the ACF modulation around the L–S spike. The vertical lines in the middle and bottom panels indicate the binary period (black dashed line)—overlapping with both the L–S and the ACF peak—and the pseudosynchronous period (red dotted line). The L–S and ACF periods are consistent with each other with the binary period and differ significantly from pseudosynchronicity.

$\log g$, and [m/H] in tandem), but the photodynamical model partially breaks this degeneracy by providing precise, independently determined surface gravities. We interpolated to these values in our analysis and were left with a more manageable $T_{\rm eff}$–[m/H] degeneracy. In principle, one could use temperatures estimated from standard photometry to help constrain the solution and overcome the $T_{\rm eff}$–[m/H] correlation, but the binary nature of the object (both stars contributing significant light) and uncertainties in the reddening make this difficult in practice. In the absence of such an external constraint, we computed a table of $T_{\rm eff,A}$ and $T_{\rm eff,B}$ values as a function of metallicity and found the highest average correlation value for [m/H] = −0.18, leading to temperatures of 6190 and 5760 K for the primary and secondary of Kepler-1647, respectively. The average flux ratio from this best fit is $F_{\rm B}/F_{\rm A} = 0.21$ at a mean wavelength of 519 nm. To arrive at the final spectroscopic parameters, we elected to resolve the remaining degeneracy by appealing to stellar evolution models.

This procedure is described below in Section 5.1 and results in slightly adjusted values of [m/H] = −0.14 ± 0.05[33] and temperatures of 6210 and 5770 K, with estimated uncertainties of 100 K.

3.3. Direct-imaging Follow-up

Due to *Kepler's* large pixel size (3.″98; Koch et al. 2010), it is possible for unresolved sources to be present inside the target's aperture and to also contaminate its light curve. A data query from MAST indicates that Kepler-1647 suffers a mean contamination of 4% ± 1% between the four seasons. To fully account for the effect this contamination has on the inferred sizes of the occulting objects, we performed an archival search and pursued additional photometric observations.

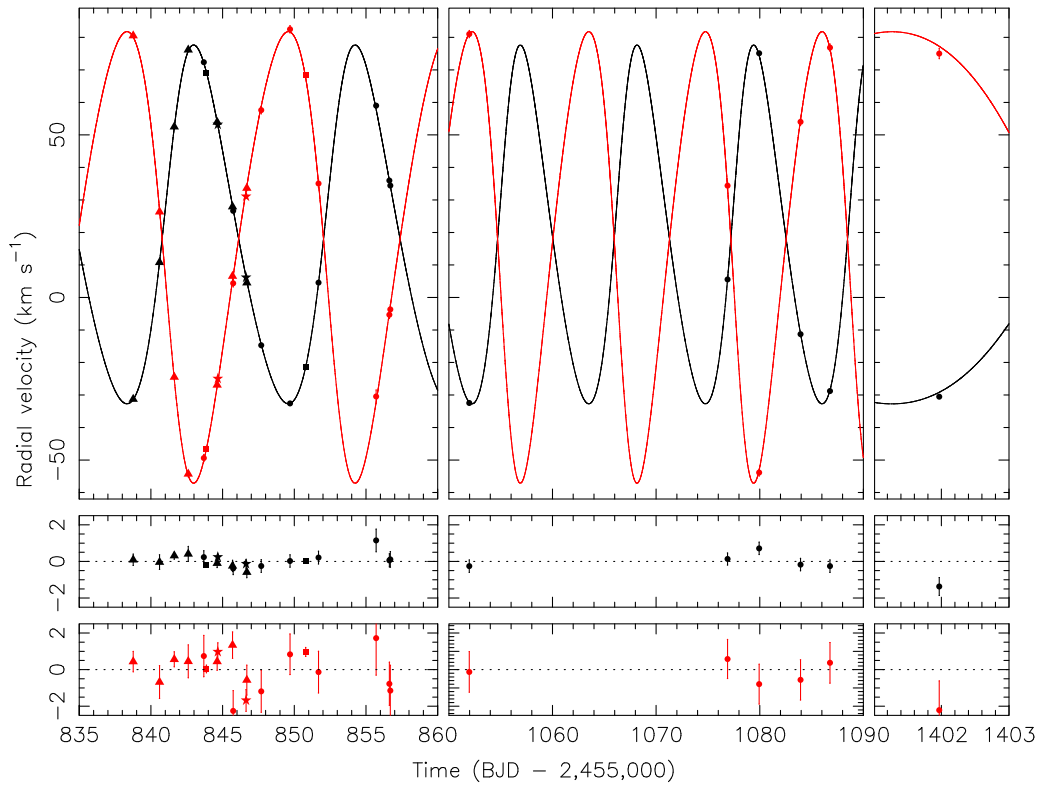[33] Note the difference from the NexSci catalog value of −0.78.

Figure 7. Top panels: radial velocity measurements for the primary (black symbols) and secondary (red symbols) stars of the EB Kepler-1647 from the McDonald 2.7 m (triangles), Lick 3 m (stars), Keck I 10 m (squares), and Tillinghast 1.5 m telescopes (circles), and the respective Keplerian fits (solid lines); bottom panels: 1σ residuals between the measured RVs and their corresponding best fits.

A nearby star to the south of Kepler-1647 is clearly resolved on UKIRT/WFCAM J-band images (Lawrence et al. 2007), with $\Delta J = 2.2$ mag and a separation of $2''.8$. Kepler-1647 was also observed in g, r, and i bands and H_α from the INT survey (Greiss et al. 2012). The respective magnitude differences between the EB and the companion are $\Delta g = 3.19$, $\Delta r = 2.73$, $\Delta H_\alpha = 2.61$, and $\Delta i = 2.52$ mag, with formal uncertainties below 1%. Based on Equations (2)–(5) from Brown et al. (2011) to convert from Sloan to K_p, these correspond to magnitude and flux differences between the EB and the companion star of $\Delta K_p = 2.73$ and $\Delta F = 8\%$. In addition, adaptive-optics observations by Dressing et al. (2014) with MMT/ARIES detected the companion at a separation of $2''.78$ from the target, with $\Delta K_s = 1.84$ mag and estimated $\Delta K_p = 2.2$ mag, and they reported a position angle for the companion of $131°.4$ (east of north).

We observed the target with WIYN/WHIRC (Meixner et al. 2010) on 2013 October 20 (UT), using a five-point dithering pattern, J, H, and K_s filters, and 30 s of integration time; the seeing was $0''.73$ (J), $0''.72$ (H), and $0''.84$ (K_s). We confirmed the presence of the companion (see Figure 8) and obtain a magnitude difference of $\Delta J = 2.21 \pm 0.04$ mag, $\Delta H = 1.89 \pm 0.06$ mag, and $\Delta K_s = 1.85 \pm 0.11$ mag, respectively. Using the formalism of Howell et al. (2012), we estimated $\Delta K_p = 2.85$ mag if the companion is a giant and $\Delta K_p = 2.9$ mag if it is a dwarf star. We adopt the latter—i.e., flux contamination of $6.9\% \pm 1.5\%$—for our pre-photodynamical analysis of the system. The position angle of the companion from our K_s-band WIYN/WHIRC images is $176°.02 \pm 0°.23$ (east of north)—consistent with the UKIRT J-band data, where the position angle of the companion is $\approx 176°$, and notably different from the results of Dressing et al. (2014).

We evaluated the probability for the companion star to be randomly aligned on the sky with Kepler-1647 using the estimates of Gilliland et al. (2011) for the number of blended background stars within a target's aperture. At the Galactic latitude of Kepler-1647 ($b = 6°.84$), there is $\approx 1.1\%$ chance for a random alignment between Kepler-1647 and a background source of $K_p \leqslant 16.45$ separated by $2''.8$, suggesting that this source is likely to be a bound companion to Kepler-1647.

As mentioned in Section 2, there is a noticeable photometric centroid shift in the photometric position of Kepler-1647 during the stellar eclipses. To investigate this, we examined the NASA Exoplanet Archive Data Validation Report (Akeson et al. 2013) for Kepler-1647. The report provides information on the location of the eclipse signal from two pixel-based methods—the photometric centroid[34] and the pixel-response function (PRF) centroid (Bryson et al. 2013).[35]

The photometric centroid of Kepler-1647 has an R.A. offset of $0''.03$ and a decl. offset of $-0''.05$ in-eclipse. The PRF difference image centroid is offset relative to the PRF OoT centroid by R.A. $= -0''.012$ and decl. $= 0''.136$, respectively (the offsets relative to the KIC position are R.A. $= -0''.019$ and decl. $= 0''.01$). Both methods indicate that the measured center

---

[34] This tracks how the center of light changes as the amount of light changes, e.g., during eclipses.
[35] This tracks the location of the eclipse source. Specifically, the centroid of the PRF difference image (the difference between the out-of transit [OoT] and in-transit images) indicates the location of the eclipse source, and the PRF OoT centroid indicates the location of the target star. Differences between these centroids provide information on the offset between the eclipse source and the target star.

Table 1
Measured Tadial Velocities

BJD$_{UTC}$ −2,455,000	RV_A (km s^{-1})	±1σ_A (km s^{-1})	RV_B (km s^{-1})	±1σ_B (km s^{-1})
843.686310 (T)[a]	72.36	0.35	−49.40	1.13
845.737695 (T)	26.66	0.34	4.36	1.11
847.691513 (T)	−14.69	0.35	57.63	1.14
849.698453 (T)	−32.58	0.34	82.50	1.11
851.685281 (T)	4.56	0.35	35.05	1.14
855.705432 (T)	59.01	0.62	−30.46	2.02
856.631747 (T)	35.98	0.36	−5.33	1.18
856.698255 (T)	34.41	0.43	−3.66	1.39
1051.968336 (T)	−32.47	0.34	81.02	1.11
1076.890883 (T)	5.54	0.33	34.40	1.07
1079.943631 (T)	75.13	0.34	−53.85	1.09
1083.935311 (T)	−11.28	0.34	54.03	1.10
1086.775726 (T)	−28.78	0.34	76.87	1.11
1401.968283 (T)	−30.52	0.49	75.03	1.60
838.762187 (M)[b]	−31.27	0.31	80.54	0.56
840.597641 (M)	10.80	0.40	26.34	0.90
842.601830 (M)	76.18	0.41	−54.28	0.90
841.625584 (M)	52.52	0.19	−24.49	0.41
844.616603 (M)	53.94	0.24	−26.92	0.48
845.691457 (M)	27.92	0.31	6.55	0.72
846.687489 (M)	4.52	0.30	33.65	0.82
844.665031 (L)[c]	53.16	0.16	−24.99	0.49
846.633214 (L)	6.15	0.23	31.05	0.59
843.869932 (K)[d]	69.07	0.08	−46.49	0.21
850.792710 (K)	−21.32	0.10	68.47	0.25

Notes.
[a] T = Fred L. Whipple Observatory, Tillinghast 1.5 m.
[b] M = McDonald Observatory, Harlan J. Smith Telescope 2.7 m.
[c] L = Lick Observatory, Shane 3 m.
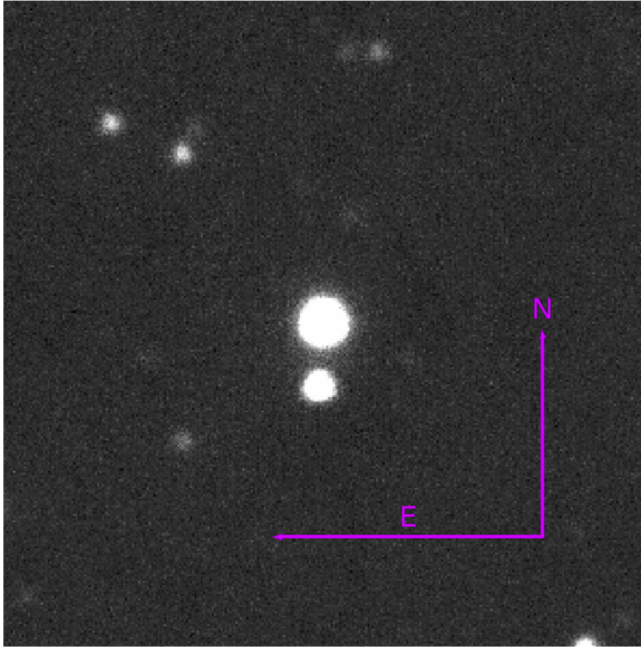[d] K = Keck Observatory.

Figure 8. *J*-band WIYN/WHIRC image of Kepler-1647 showing the nearby star to the south of the EB. The size of the box is 30″ by 30″. The two stars are separated by 2″89 ± 0″14.

of light shifts away from Kepler-1647 during the stellar eclipses, fully consistent with the photometric contamination from the companion star to the SE of the EB. There is no apparent centroid shift during the planetary transits, indicating that these are indeed caused by a CBP in orbit around Kepler-1647.

3.4. Time-series Photometric Follow-up

In order to confirm the model derived from the *Kepler* data and to place additional constraints on the model over a longer time baseline, we undertook additional time-series observations of Kepler-1647 using the KELT follow-up network, which consists of small and midsize telescopes used for confirming transiting planets for the KELT survey (Pepper et al. 2007; Siverd et al. 2012). Based on predictions of primary eclipse times for Kepler-1647, we obtained two observations of partial eclipses after the end of the *Kepler* primary mission. The long durations of the primary eclipse (>9 hr) make it nearly impossible to completely observe from any one site, but partial eclipses can nevertheless help constrain the eclipse time.

We observed a primary eclipse simultaneously in *V* and *i* at Swarthmore College's Peter van de Kamp Observatory on UT2013-08-17. The observatory uses a 0.6 m RCOS Telescope with an Apogee U16M 4 K × 4 K CCD, giving a 26′ × 26′ field of view. Using 2 × 2 binning, it has 0″76/pixel. These observations covered the second half of the eclipse, extending about 2.5 hr after egress.

We observed a primary eclipse of the system at Canela's Robotic Observatory (CROW) in Portugal. Observations were made using a 0.3 m LX200 telescope with an SBIG ST-8XME CCD. The FOV is 28′ × 19′ and 1″11/pixel. Observations were taken on UT2015-08-18 using a clear, blue-blocking (CBB) filter. These observations covered the second half of the eclipse, extending about 1 hr after egress. The observed eclipses from KELT, shown in Figure 9, match well with the forward photodynamical models (Section 4.2).

To complement the *Kepler* data, we used the 1 m Mount Laguna Observatory telescope to observe Kepler-1647 at the predicted times for planetary transits in the summer of 2015 (see Table 2). Suboptimal observing conditions thwarted our efforts and, unfortunately, we were unable to detect the transits. The obtained images, however, confirmed the presence and orientation of the nearby star to the south of Kepler-1647.

4. UNRAVELING THE SYSTEM

Kepler-1647b produced three transits: two across the secondary star at $t_{B,1}$ = −3.0018 and $t_{B,2}$ = 1109.2612 (BJD–2,455,000), corresponding to EB phase of 0.60 and 0.39, respectively, and one heavily blended transit across the primary star at time $t_{A,1}$—a syzygy (the secondary star and the planet simultaneously cross the line of sight between *Kepler* and the disk of the primary star) during a primary stellar eclipse at t_{prim} = 1104.8797. The latter transit is not immediately obvious and requires careful inspection of the light curve. We measured transit durations across the secondary of $t_{dur,B,1}$ = 0.137 days and $t_{dur,B,2}$ = 0.279 days. The light curve and the configuration of the system at the time of the syzygy are shown in Figure 10.
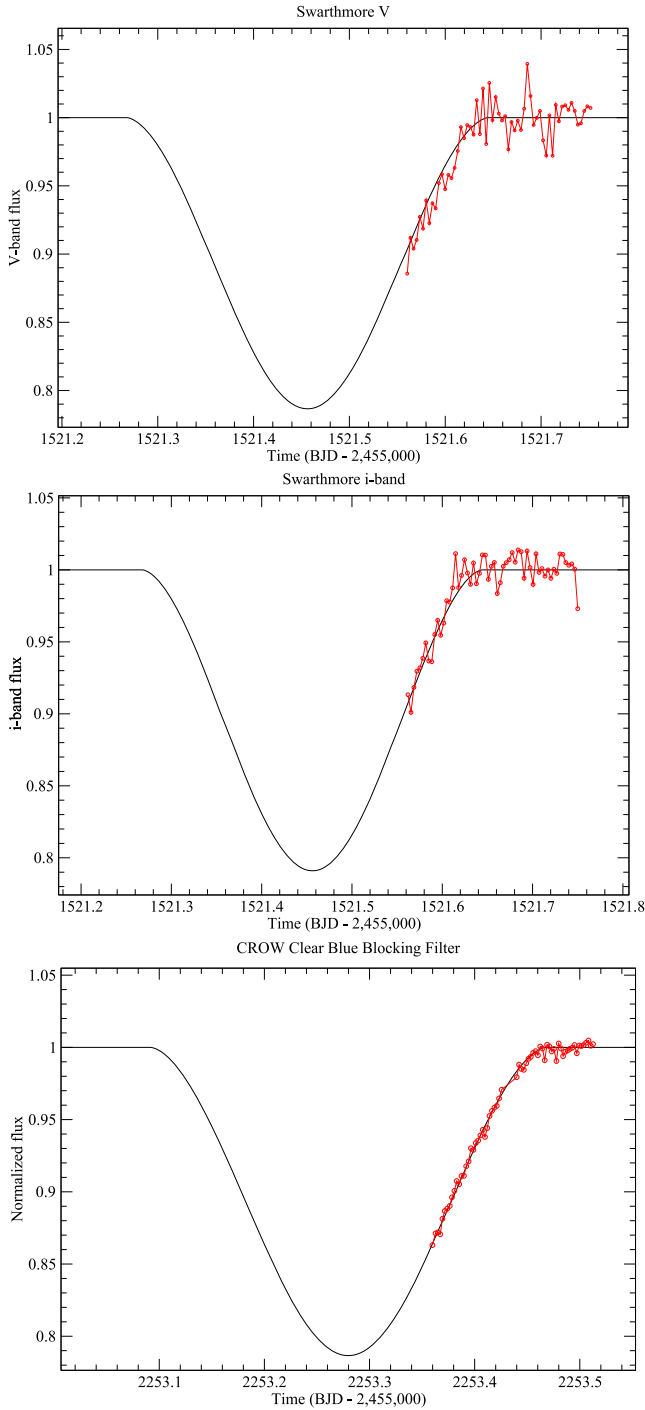
Figure 9. Observed (KELT network data; red symbols) and photodynamically predicted (solid line) primary eclipses of Kepler-1647. The top panel is for Swarthmore *V* band, the middle panel is for Swarthmore *i* band, and the bottom panel is for CROW observatory CBB filter (see text for details). The data are fully consistent with the photodynamical predictions.

To extract the transit center time and duration across the primary star, t_A and $t_{dur,A}$, we subtracted a primary eclipse template from the data and then measured the mid-transit time and duration from the residual light curve—now containing only the planetary transit—to be $t_A = 1104.9510$ (BJD–2,455,000), corresponding to EB phase 0.006, and $t_{dur,A} = 0.411$ days. From the transit depths, and accounting

for dilution, we estimated $k_{p,prim} = R_p/R_A = 0.06$ and $k_{p,sec} = R_p/R_B = 0.11$. We outline the parameters of the planetary transits in Table 2. As expected from a CBP, the two transits across the secondary star vary in both depth and duration, depending on the phase of the EB at the respective transit times. This unique observational signature rules out common false positives (such as a background EB) and confirms the nature of the planet. In the following section we describe how we used the center times and durations of these three CBP transits to analytically describe the planet's orbit.

4.1. Analytic Treatment

As discussed in Schneider & Chevreton (1990) and Kostov et al. (2013), the detection of CBP transits across one or both stars during the same inferior conjunction (e.g., Kepler -34, Kepler-35, and now Kepler-1647) can strongly constrain the orbital configuration of the planet when the host system is an SB2 EB. Such a scenario, dubbed "double-lined, double-dipped" (Kostov et al. 2013), is optimal in terms of constraining the a priori unknown orbit of the CBP.

4.1.1. CBP Transit Times

Using the RV measurements of the EB (Table 1) to obtain the *x*- and *y*-coordinates of the two stars at the times of the CBP transits, and combining these with the measured time interval between two consecutive CBP transits, we can estimate the orbital period and semimajor axis of the CBP—independent of and complementary to the photometric-dynamical model presented in the next section. Specifically, the CBP travels a known distance Δx for a known time Δt between two consecutive transits across either star (but during the same inferior conjunction), and its *x*-component velocity is[36]

$$V_{x,p} = \frac{\Delta x}{\Delta t}$$
$$\Delta x = |x_i - x_j|$$
$$\Delta t = |t_i - t_j| \qquad (2)$$

where $x_{i,j}$ is the *x*-coordinate of the star being transited by the planet at the observed mid-transit time of $t_{i,j}$. As described above, the CBP transited across the primary and secondary star during the same inferior conjunction, namely, at $t_i = t_A = 1104.9510 \pm 0.0041$ and at $t_j = t_{B,2} = 1109.2612 \pm 0.0036$ (BJD–2,455,000). Thus, $\Delta t = 4.3102 \pm 0.0055$ days.

The barycentric *x*-coordinates of the primary and secondary stars are (Hilditch 2001)[37]

$$x_{A,B}(t_{A,B}) = r_{A,B}(t_{A,B})\cos[\theta_{A,B}(t_{A,B}) + \omega_{bin}] \qquad (3)$$

where $r_{A,B}(t_{A,B})$ is the radius vector of each star at the times of the CBP transits t_A and $t_{B,2}$:

$$r_{A,B}(t_{A,B}) = a_{A,B}(1 - e_{bin}^2)[1 + e_{bin}\cos(\theta_{A,B}(t_{A,B}))]^{-1} \qquad (4)$$

where $\theta_{A,B}(t_{A,B})$ are the true anomalies of the primary and secondary stars at t_A and t_B, and $e_{bin} = 0.159 \pm 0.003$ and $\omega_{bin} = 300°.85 \pm 0°.91$ are the binary eccentricity and argument

---

[36] The observer is at $+z$, and the sky is in the *xy* plane.
[37] The longitude of ascending node of the binary star, Ω_{bin}, is undefined and set to zero throughout this paper.
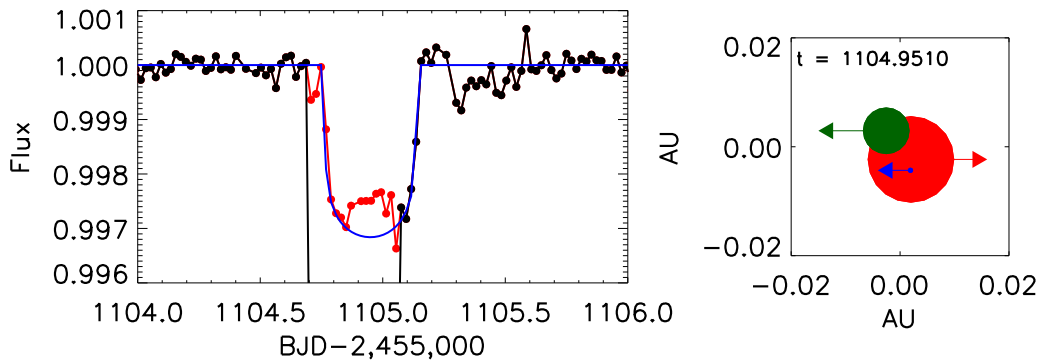
Figure 10. *Kepler* LC light curve (left panel) and the configuration (right panel) of the Kepler-1647 system at the time of the syzygy shortly after a primary stellar eclipse. The planet does not cross the disk of the secondary star—the configuration of the system and the sizes of the objects on the right panel are to scale, and the arrows indicate their sky-projected direction of motion. The red symbols in the left panel represent the light curve after removal of a primary eclipse template; the blue curve in the left panel represents the fit to the transit of the CBP across the primary star. The suboptimal fit to the depth of the planetary transit is due to imperfect removal of the stellar eclipse caused by noisy data.

of periastron, respectively, as derived from the spectroscopic measurements (see Table 1). Using the measured semiamplitudes of the RV curves for the two host stars ($K_A = 55.73 \pm 0.21$ km s^{-1} and $K_B = 69.13 \pm 0.5$ km s^{-1}; see Table 1) and the binary period $P_{bin} = 11.2588$ days, the semimajor axes of the two stars are $a_A = 0.0569 \pm 0.0002$ AU and $a_B = 0.0707 \pm 0.0005$ AU, respectively (Equation (2.51) of Hilditch 2001).

To find $\theta_{A,B}(t_{A,B})$, we solved *Kepler*'s equation for the two eccentric anomalies,[38] $E_{A,B} - e_{bin} \sin(E_{A,B}) = 2\pi (t_{A,B} - t_0)/P_{bin}$, where $t_0 = -47.869 \pm 0.003$ (BJD − 2, 455, 000) is the time of periastron passage for the EB, and obtain $\theta_A(t_A) = 2.64 \pm 0.03$ rad, $\theta_B(t_{B,2}) = 4.55 \pm 0.03$ rad. The radius vector of each star is then $r_A(t_A) = 0.065 \pm 0.003$ AU and $r_B(t_B) = 0.071 \pm 0.004$ AU, and from Equation (3), $x_A(t_A) = 0.0020 \pm 0.0008$ AU and $x_B(t_B) = -0.0658 \pm 0.0009$ AU. Thus, $\Delta x = 0.0681 \pm 0.0012$ AU and, finally, $V_{x,p} = 0.0158 \pm 0.0006$ AU/day (see Equation (2)).

Next, we used $V_{x,p}$ to estimate the period and semimajor axes of the CBP as follows. The x-component of the planet's velocity, assuming that $\cos(\Omega_p) = 1$ and $\cos(i_p) = 0$ (where Ω_p and i_p are the planet's longitude of ascending node and inclination, respectively, in the reference frame of the sky),[39] is

$$V_{x,p} = -\left(\frac{2\pi G M_{bin}}{P_p}\right)^{1/3} \frac{[e_p \sin \omega_p + \sin(\theta_p + \omega_p)]}{\sqrt{(1 - e_p^2)}} \quad (5)$$

where $M_{bin} = 2.19 \pm 0.02\, M_\odot$ is the mass of the binary star (calculated from the measured radial velocities of its two component stars—Equation (2.52) of Hilditch 2001) and P_p, e_p, ω_p, and θ_p are the orbital period, eccentricity, argument of periastron, and true anomaly of the planet, respectively. When the planet is near inferior conjunction, like during the transits at t_A and $t_{B,2}$, we can approximate $\sin(\theta_p + \omega_p) = 1$. Simple algebra shows that

$$P_p = 1080 \frac{(1 + e_p \sin \omega_p)^3}{(1 - e_p^2)^{3/2}} \text{ [days]}. \quad (6)$$

Thus, if the orbit of Kepler-1647b is circular, its orbital period is $P_p \approx 1100$ days and its semimajor axis is $a_p \approx 2.8$ AU. In this case we can firmly rule out a CBP period of 550 days.

Even if the planet has a nonzero eccentricity, Equation (6) still allowed us to constrain the orbit it needs to produce the two transits observed at t_A and $t_{B,2}$. In other words, if P_p is indeed not ∼1100 days but half of that (assuming that a missed transit fell into a data gap), then from Equation (6)

$$2(1 + e_p \sin \omega_p)^3 = (1 - e_p^2)^{3/2} \leqslant 1, \quad (7)$$

which implies $e_p \geqslant 0.21$. Thus, Equation (7) indicates that unless the eccentricity of CBP Kepler-1647b is greater than 0.21, its orbital period cannot be half of 1100 days.

We note that our Equation (7) differs from Equation (8) in Schneider & Chevreton (1990) by a factor of $4\pi^3$. As the two equations describe the same phenomenon (for a circular orbit for the planet), we suspect that there is a missing factor of 2π in the sine and cosine parts of their Equations (6a) and (6b), which propagated through.

4.1.2. CBP Transit Durations

As shown by Kostov et al. (2013, 2014) for the cases of Kepler-47b, Kepler-64b, and Kepler-413b and discussed by Schneider & Chevreton (1990), the measured transit durations of CBPs can constrain the a priori unknown mass of their host binary stars[40] when the orbital period of the planets can be estimated from the data. The case of Kepler-1647 is the opposite—the mass of the EB is known (from spectroscopic observations), while the orbital period of the CBP cannot be pinned down prior to a full photodynamical solution of the system. However, we can still estimate the orbital period of Kepler-1647b using its transit durations:

$$t_{dur,n} = \frac{2 R_{c,n}}{V_{x,p} + V_{x,star,n}} \quad (8)$$

where $R_{c,n} = R_{star,n}\sqrt{(1 + k_p)^2 - b_n^2}$ is half the transit chord (where $k_{p,prim} = 0.06$, $k_{p,sec} = 0.11$, and b_n is the impact parameter) for the nth CBP transit and $V_{x,star,n}$ and $V_{x,p}$ are the x-component velocities of the star and of the CBP, respectively. Using Equation (5), we can rewrite Equation (8)

---

[38] Taking into account that ω for the primary star is $\omega_{bin} - \pi$.
[39] Both consistent with the planet transiting near inferior conjunction.

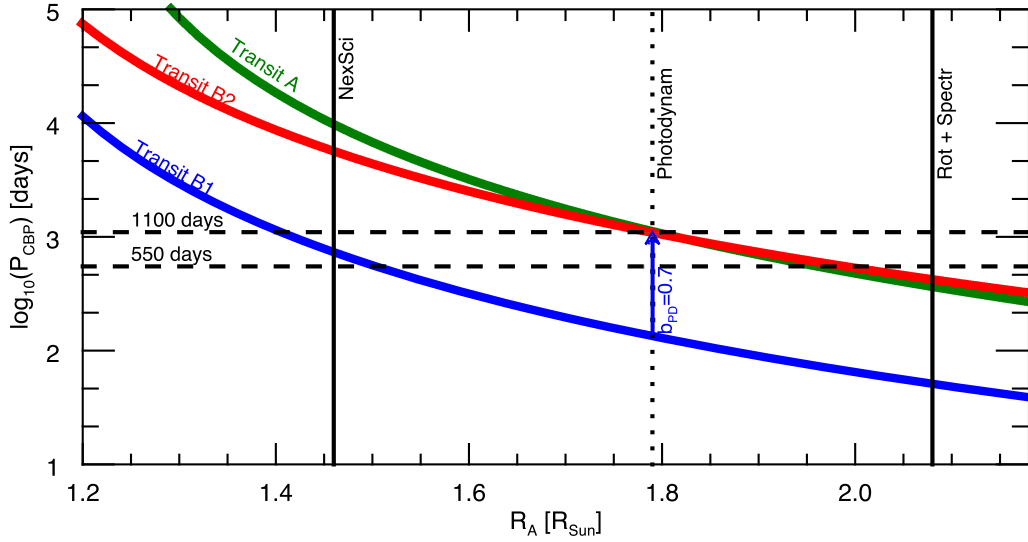[40] Provided that they are single-lined spectroscopic binaries.

Figure 11. Analytic constraints on the minimum allowed period of the CBP (the region above each solid line, Equation (10)), as a function of the measured transit durations and the a priori uncertain primary radius (R_A) and assuming a circular CBP orbit. The colors of the solid lines correspond to transit A (green), transit B2 (red), and transit B1 (blue). The uppermost curve for each radius constrains the minimum period the most. From left to right, the dotted vertical lines represent the primary radius provided by NexSci, calculated from our photodynamical model, and inferred from our rotation and spectroscopy analysis. To be consistent with the data, R_A must be larger than ~1.75 $R_\odot$, and the impact parameter of transit B1 must be large—in line with the photodynamical solution of the system. Accounting for the photodynamically measured impact parameter for transit B1 (blue arrow) makes the analytically derived period of the planet fully consistent with the numerically derived value of ~1100 days.

in terms of P_p (the orbital period of the planet) near inferior conjunction ($\sin(\theta_p + \omega_p) = 1$) as

$$P_p(t_{dur,n})$$
$$= 2\pi G M_{bin}(1 + e_p \sin \omega_p)^3 \left(\frac{2R_{c,n}}{t_{dur,n}} - V_{x,star,n}\right)^{-3}(1 - e_p^2)^{-3}$$
(9)

where the stellar velocities $V_{x,star,n}$ can be calculated from the observables (see Equation (3) of Kostov et al. 2013): $V_{x,A} = 2.75 \times 10^{-2}$ AU/day, $V_{x,B,1} = 4.2 \times 10^{-2}$ AU/day, and $V_{x,B,2} = 2 \times 10^{-2}$ AU/day. Using the measured values for $t_{dur,A}$, $t_{dur,B,1}$, and $t_{dur,B,2}$ (listed in Table 2) and requiring $b_n \geqslant 0$, for a circular orbit of the CBP we obtained

$$P_p(t_{dur,A}) \text{ [days]} \geqslant 4076 \times \left(2.4\left(\frac{R_A}{R_\odot}\right) - 2.75\right)^{-3}$$

$$P_p(t_{dur,B,1}) \text{ [days]} \geqslant 4076 \times \left(4.1\left(\frac{R_A}{R_\odot}\right) - 4.2\right)^{-3}$$

$$P_p(t_{dur,B,2}) \text{ [days]} \geqslant 4076 \times \left(2\left(\frac{R_A}{R_\odot}\right) - 2\right)^{-3}.$$
(10)

We show these inequalities, defining the allowed region for the period of the CBP as a function of the (a priori uncertain) primary radius, in Figure 11. The allowed regions for the CBP period are above each of the solid lines (green for transit A, red for transit B2, and blue for transit B1), where the uppermost line provides the strongest lower limit for the CBP period at the specific R_A. The dotted vertical lines denote, from left to right, the radius provided by NexSci ($R_{A,NexSci} = 1.46\,R_\odot$), calculated from our photodynamical model ($R_{A,PD} = 1.79\,R_\odot$; Section 4.2), and inferred from the rotation period ($R_{A,rot} = 2.08\,R_\odot$). As seen from the figure, $R_{A,NexSci}$ is too

small as the corresponding minimum CBP periods are too long —if this was indeed the primary stellar radius, then the measured duration of transit A (the strongest constraint at that radius) would correspond to $P_{CBP} \sim 10^4$ days (for a circular orbit). The rotationally inferred radius is consistent with a planet on either a 550-day orbit or an 1100-day orbit, but given its large uncertainty (see Section 2.2), the constraint it provides on the planet period is rather poor.

Thus, while the measured transit durations cannot strictly break the degeneracy between a 550-day and an 1100-day CBP period prior to a full numerical treatment, they provide useful constraints. Specifically, without any prior knowledge of the transit impact parameters and only assuming a circular orbit, Equation (9) indicates that (a) the impact parameter of transit B1 must be large (in order to bring the blue curve close to the other two) and (b) R_A must be greater than ~1.75 $R_\odot$ (where the green and red lines intersect) so that the three inequalities in Equation (10) are consistent with the data.

We note that P_p in Equation (9) is highly dependent on the impact parameter of the particular CBP transit (which is unknown prior to a full photodynamical solution). Thus, a large value for $b_{B,1}$ will bring the transit B1 curve (blue) closer to the other two. Indeed, our photodynamical model indicates that $b_{B,1} \approx 0.7$, corresponding to $P_p(t_{dur,B,1}) = 1105$ days from Equation (9) (also blue arrow in Figure 11)—bringing the blue curve in line with the other two and validating our analytic treatment of the transit durations. The other two impact parameters, $b_{A,1}$ and $b_{B,2}$, are both ≈0.2 according to the photodynamical model, and they do not significantly affect Equation (9) since their contribution is small (i.e., $b_A^2 \approx b_{B,2}^2 \approx 0.04$). For the photodynamically calculated $R_{A,PD} = 1.79\,R_\odot$, the respective analytic CBP periods are $P_p(t_{dur,A}) = 1121$ days and $P_p(t_{dur,B,2}) = 1093$ days. Thus, the analytic analysis presented here is fully consistent with the comprehensive numerical solution of the system, which we present in the next section.

4.2. Photometric-dynamical Solution

CBPs reside in dynamically rich, multi-parameter space where a strictly Keplerian solution is not adequate. A comprehensive description of these systems requires a full photometric-dynamical treatment based on the available and follow-up data, on N-body simulations, and on the appropriate light-curve model. We describe this treatment below.

4.2.1. Eclipsing Light Curve (ELC)

To obtain a complete solution of the Kepler-1647 system, we used the ELC code (Orosz & Hauschildt 2000) with recent "photodynamical" modifications (e.g., Welsh et al. 2015). The code fully accounts for the gravitational interactions between all bodies. Following Mardling & Lin (2002), the gravitational force equations have been modified to account for precession due to general relativistic (GR) effects and due to tides.

Given initial conditions (e.g., masses, positions, and velocities for each body), the code utilizes a 12th-order symplectic Gaussian Runge–Kutta integrator (Hairer et al. 2003) to calculate the three-dimensional positions and velocities of the two stars and the planet as a function of time. These are combined with the light-curve model of Mandel & Agol (2002) and the quadratic law limb-darkening coefficients, using the "triangular" sampling of Kipping (2013), to calculate model light and radial velocity curves, which are directly compared to the *Kepler* data (both LC and, where available, SC), the measured stellar radial velocities, and the ground-based light curves.

The ELC code uses the following as adjustable parameters: the three masses and three sizes of the occulting objects, the Keplerian orbital elements (in terms of Jacobian coordinates) for the EB and the CBP (e_{bin}, e_p, i_{bin}, i_p, ω_{bin}, ω_p, P_{bin}, P_p, and times of conjunction $T_{c,bin}$, $T_{c,p}$),[41] the CBP longitude of ascending node Ω_p (Ω_{bin} is undefined and set to zero throughout), the ratio between the stellar temperatures, the quadratic limb-darkening coefficients of each star in the *Kepler* bandpass and primary limb-darkening coefficients for the three bandpasses used for the ground-based observations, and the seasonal contamination levels of the *Kepler* data. The GR modifications to the force equations require no additional parameters, and the modifications to account for apsidal motion require the so-called k_2 constant and the ratio of the rotational frequency of the star to its pseudosynchronous value for each star. For fitting purposes, we used parameter composites or ratios (e.g., $e \cos \omega$, $e \sin \omega$, M_A/M_B, R_A/R_B) as these are generally better constrained by the data. We note that the parameters quoted here are the instantaneous "osculating" values. The coordinate system is Jacobian, so the orbit of the planet is referred to the center of mass of the binary star. These values are valid for the reference epoch only since the orbits of the EB and the CBP evolve with time, and must be used in the context of a dynamical model to reproduce our results.

As noted earlier, starspot activity is evident in the *Kepler* light curve. After some initial fits, it was found that some of the eclipse profiles were contaminated by starspot activity. We carefully examined the residuals of the fit and selected five primary and five secondary eclipses that have "clean" residuals (these are shown in Figure 2). We fit these clean profiles, the

times of eclipse for the remaining eclipse events (corrected for starspot contamination), the three ground-based observations, and the two radial velocity curves. We used the observed rotational velocities of each star and the spectroscopically determined flux ratio between the two stars (see Table 3) as additional constraints. The model was optimized using a Differential Evolution Monte Carlo Markov Chain (DE-MCMC; ter Braak & Vrugt 2006). A total of 161 chains were used, and 31,600 generations were computed. We skipped the first 10,000 generations for the purposes of computing the posterior distributions. We adopted the parameters from the best-fitting model and use posterior distributions to get the parameter uncertainties.

Throughout the text we quote the best-fit parameters. These do not have error bars and, as noted above, should be interpreted strictly as the parameters reproducing the light curve. For uncertainties the reader should refer to the mode and the mean values calculated from the posterior distributions.

4.2.2. Consistency Check

We confirmed the ELC solution with the *photodynam* code (Carter et al. 2011, previously used for a number of CBPs; e.g., Doyle et al. 2011; Welsh et al. 2012; Schwamb et al. 2013; Kostov et al. 2014). We note, however, that the *photodynam* code does not include tidal apsidal motion—which must be taken into account for Kepler-1647 as discussed above. Thus, while the solution of the *photodynam* code provides adequate representation of the light curve of Kepler-1647 (the differences are indistinguishable by eye), it is not the best-fit model in terms of chi-square statistics. We outline the input for the *photodynam* code[42] required to reproduce the light curve of Kepler-1647 in Table 6.

We also carried out an analysis using an independent photodynamical code (developed by coauthor D.R.S.) that is based on the Nested Sampling concept. This code includes both GR and tidal distortion. Nested Sampling was introduced by Skilling (2004) to compute the Bayesian Evidence (marginal likelihood or the normalizing factor in Bayes' theorem). As a by-product, a representative sample of the posterior distribution is also obtained. This sample may then be used to estimate the statistical properties of parameters and of derived quantities of the posterior. MultiNest was an implementation by Feroz et al. (2008) of Nested Sampling incorporating several improvements. Our version of MultiNest is based on the Feroz code and is a parallel implementation. The MultiNest solution confirmed the ELC solution.

5. RESULTS AND DISCUSSION

The study of extrasolar planets is first and foremost the study of their parent stars, and transiting CBPs, in particular, are a prime example. As we discuss in this section,[43] their peculiar observational signatures, combined with *Kepler's* unmatched precision, help us to not only decipher their host systems by a comprehensive photodynamical analysis but also constrain the fundamental properties of their host stars to great precision. In essence, transiting CBPs allow us to extend the "royal road" of EBs (Russell 1948) to the realm of exoplanets.

---

[41] The time of conjunction is defined as the conjunction with the barycenter of the system. For the EB, this is close to a primary eclipse, while the CBP does not necessarily transit at conjunction.

[42] In terms of osculating parameters.

[43] And also shown by the previous *Kepler* CBPs.

Table 2
Mid-transit Times, Depths, and Durations of the Planetary Transits

Event #	Center (Time-2455000 [BJD])	σ (Center)	Depth[a] (ppm)	σ (Depth)	Duration (days)	σ (Duration)	Center (Time-2,455,000 [BJD])	Depth (ppm)	Duration (days)
Observed							*Predicted*		
1	−3.0018	0.0027	2070	150	0.1352	0.0125	−3.0035	2080	0.1278
2	1104.9510	0.0041	2990	250	0.4013	0.0071	1104.9515	3210	0.3973
3	1109.2612	0.0036	2470	70	0.2790	0.0088	1109.2645	2450	0.2727
Future									
4[b]	⋯	⋯	⋯	⋯	⋯	⋯	2209.5440	3200	0.4250
5[b]	⋯	⋯	⋯	⋯	⋯	⋯	2213.7253	2460	0.1756
6[c]	⋯	⋯	⋯	⋯	⋯	⋯	3314.5362	3000	0.6597
7[c]	⋯	⋯	⋯	⋯	⋯	⋯	3317.4837	2860	0.6840
8[c]	⋯	⋯	⋯	⋯	⋯	⋯	3317.9441	2390	0.1517
9[c]	⋯	⋯	⋯	⋯	⋯	⋯	3321.0339	3290	0.5604

Notes.
[a] In terms of $(r_p/r_A)^2$.
[b] Unsuccessful attempts to observe from the ground.
[c] Within the operation time frame of the *TESS* mission (i.e., 2018 July 14, 17, and 21).
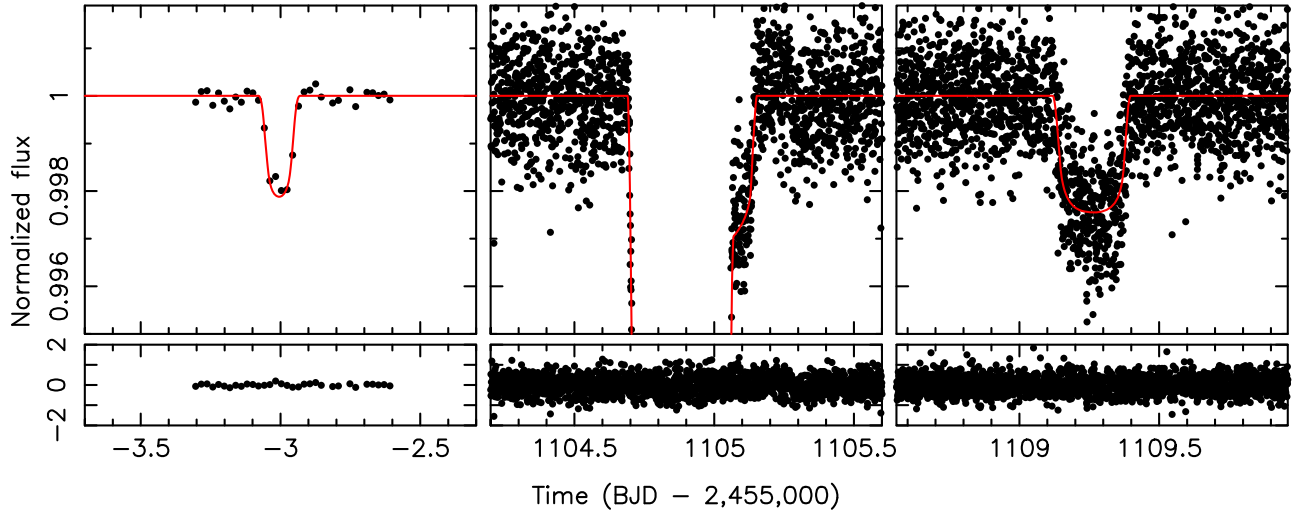
Figure 12. ELC photodynamical solution (red, or gray color) for the normalized *Kepler* light curve (black symbols) of Kepler-1647, centered on the three transits of the CBP, and the respective residuals. The left panel shows LC data; the middle and right panels show SC data. The first and third transits are across the secondary star, and the second transit (heavily blended with a primary stellar eclipse off the scale of the panel) is across the primary star—during a syzygy. The model represents the data well.

5.1. The Kepler-1647 System

Our best-fit ELC photodynamical solutions for Kepler-1647 and the orbital configuration of the system are shown in Figures 12 and 13, respectively. The correlations between the major parameters are shown in Figure 14. The ELC model parameters are listed in Tables 3 (fitting parameters), 4 (derived Keplerian elements), and 5 (derived Cartesian). Table 3 lists the mode and mean of each parameter, as well as their respective uncertainties as derived from the MCMC posterior distributions; the upper and lower bounds represent the 68% range. The subpercent precision on the stellar masses and sizes (see the respective values in Table 4) demonstrates the power of photodynamical analysis of transiting CB systems. The parameters presented in Tables 4 and 5 represent the osculating, best-fit model to the *Kepler* light curve and are

only valid for the reference epoch (BJD–2,455,000). These are the parameters that should be used when reproducing the data. The mid-transit times, depths, and durations of the observed and modeled planetary transits are listed in Table 2.

The central binary Kepler-1647 is host to two stars with masses of $M_A = 1.2207 \pm 0.0112\,M_\odot$ and $M_B = 0.9678 \pm 0.0039\,M_\odot$ and radii of $R_A = 1.7903 \pm 0.0055\,R_\odot$ and $R_B = 0.9663 \pm 0.0057\,R_\odot$, respectively (Table 4). The temperature ratio of the two stars is $T_B/T_A = 0.9365 \pm 0.0033$, and their flux ratio is $F_B/F_A = 0.21 \pm 0.02$ in the *Kepler* bandpass. The two stars of the binary revolve around each other every 11.25882 days in an orbit with a semimajor axis of $a_{bin} = 0.1276 \pm 0.0002$ AU, eccentricity of $e_{bin} = 0.1602 \pm 0.0004$, and inclination of $i_{bin} = 87°9164 \pm 0°0145$ (see also Table 4 for the respective mean and mode values).
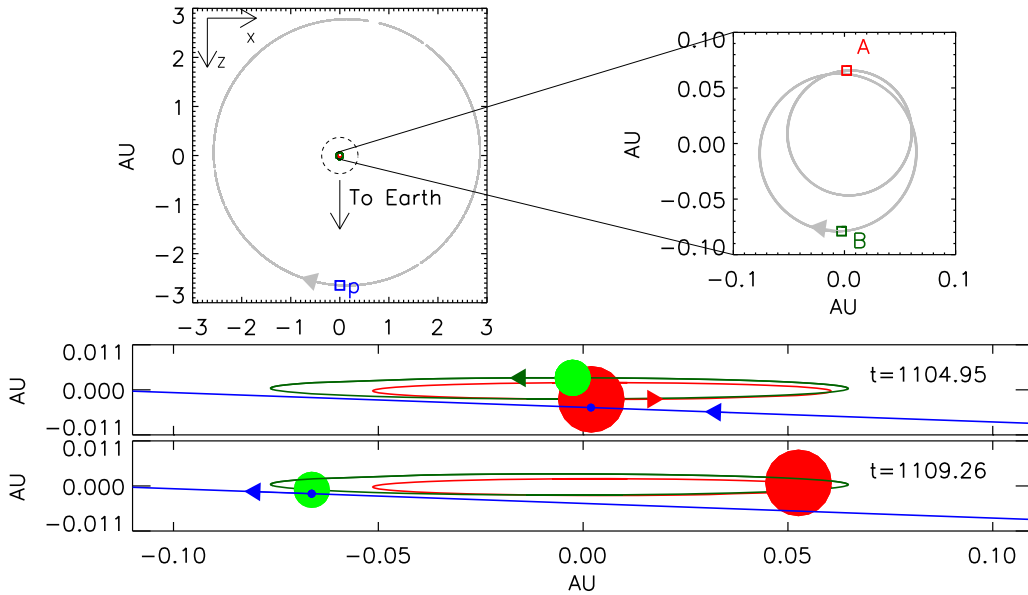
Figure 13. ELC photodynamical solution for the orbital configuration of the Kepler-1647b system. The orbits and the symbols for the two stars in the bottom two panels (red, or dark color for primary "A," green, or light color for the secondary "B") are to scale; the planet symbols in the bottom two panels (blue color) are exaggerated by a factor of two for viewing purposes. The top two panels show the configuration of the system at $t_A = 1104.95$ (BJD–2,455,000) as seen from above; the dashed line in the top left panel represents the minimum distance from the EB for dynamical stability. The bottom two panels show the configuration of the system (and the respective directions of motion) at two consecutive CBP transits during the same conjunction for the planet: at $t_A = 1104.95$ and at $t_{B,2} = 1109.26$ (BJD–2,455,000). The orientation of the xz coordinate axes (using the nomenclature of Murray & Correia 2011, pp. 15–23) is indicated in the upper left corner of the top left panel.

The accurate masses and radii of the Kepler-1647 stars, along with our constraints on the temperatures and metallicity of this system, enable a useful comparison with stellar evolution models. As described in Section 3.2, a degeneracy remains in our determination of [m/H] and $T_{\rm eff}$, which we resolved here by (1) noting that current models are typically found to match the observed properties of main-sequence F stars fairly well (see, e.g., Torres et al. 2010) and (2) making the working assumption that the same should be true for the primary of Kepler-1647, of spectral type approximately F8. We computed model isochrones from the Yonsei-Yale series (Yi et al. 2001; Demarque et al. 2004) for a range of metallicities. In order to properly compare results from theory and observation, at each value of metallicity, we also adjusted the spectroscopic temperatures of both stars by interpolation in the table of $T_{\rm eff,A}$ and $T_{\rm eff,B}$ versus [m/H] mentioned in Section 3.2. This process led to an excellent fit to the primary star properties (mass, radius, temperature) for a metallicity of [m/H] $= -0.14$ $\pm$ 0.05 and an age of 4.4 $\pm$ 0.25 Gyr. This fit is illustrated in the mass–radius and mass–temperature diagrams of Figure 15. We found that the temperature of the secondary is also well fit by the same model isochrone that matches the primary. The radius of the secondary, however, is only marginally matched by the same model and appears nominally larger than predicted at the measured mass. Evolutionary tracks for the measured masses and the same best-fit metallicity are shown in Figure 16.

One possible cause for the slight tension between the observations and the models for the secondary in the mass–radius diagram is a bias in either the measured masses or the radii. While the individual masses may indeed be subject to systematic uncertainty, the mass *ratio* should be more accurate, and a horizontal shift in the top panels of Figure 15 can only improve the agreement with the secondary at the expense of the primary. Similarly, the sum of the radii is tightly constrained by the photodynamical fit, and the good agreement between the

spectroscopic and photometric estimates of the flux ratio (see Table 7) is an indication that the radius ratio is also accurate. The flux ratio is a very sensitive indicator because it is proportional to the square of the radius ratio.

An alternative explanation for this tension may be found in the physical properties of the secondary star. As discussed in Section 2.2, Kepler-1647 B is an active star with a rotation period of 11 days. In addition, the residuals from the times of eclipse (Figure 4) provide evidence of spots on the surface of this star, likely associated with strong magnetic fields. Such stellar activity is widely believed to be responsible for "radius inflation" among stars with convective envelopes (see, e.g., Torres 2013). The discrepancy between the measured and predicted radius for the radius of Kepler-1647 B amounts to 0.014 $R_\odot$ (1.4%), roughly 2.5 times the radius uncertainty at a fixed mass. Activity-induced radius inflation also generally causes the temperatures of late-type stars to be too cool compared to model predictions. This "temperature suppression" is, however, not seen in the secondary star of Kepler-1647, possibly because of systematic errors in our spectroscopic temperatures or because the effect may be smaller than our uncertainties. We note that while radius and temperature discrepancies are more commonly seen in M dwarfs, the secondary of Kepler-1647 is not unique in showing some of the same effects despite being much more massive (only ∼3% less massive than the Sun). Other examples of active stars of similar mass to Kepler-1647 B with evidence of radius inflation and sometimes temperature suppression include V1061 Cyg B (Torres et al. 2006), CV Boo B (Torres et al. 2008), V636 Cen B (Clausen et al. 2009), and EF Aqr B (Vos et al. 2012). In some of these systems, the effect is substantially larger than that in Kepler-1647 B and can reach up to 10%.

We note that while the best-fit apsidal constant for the primary star is consistent with the corresponding models of
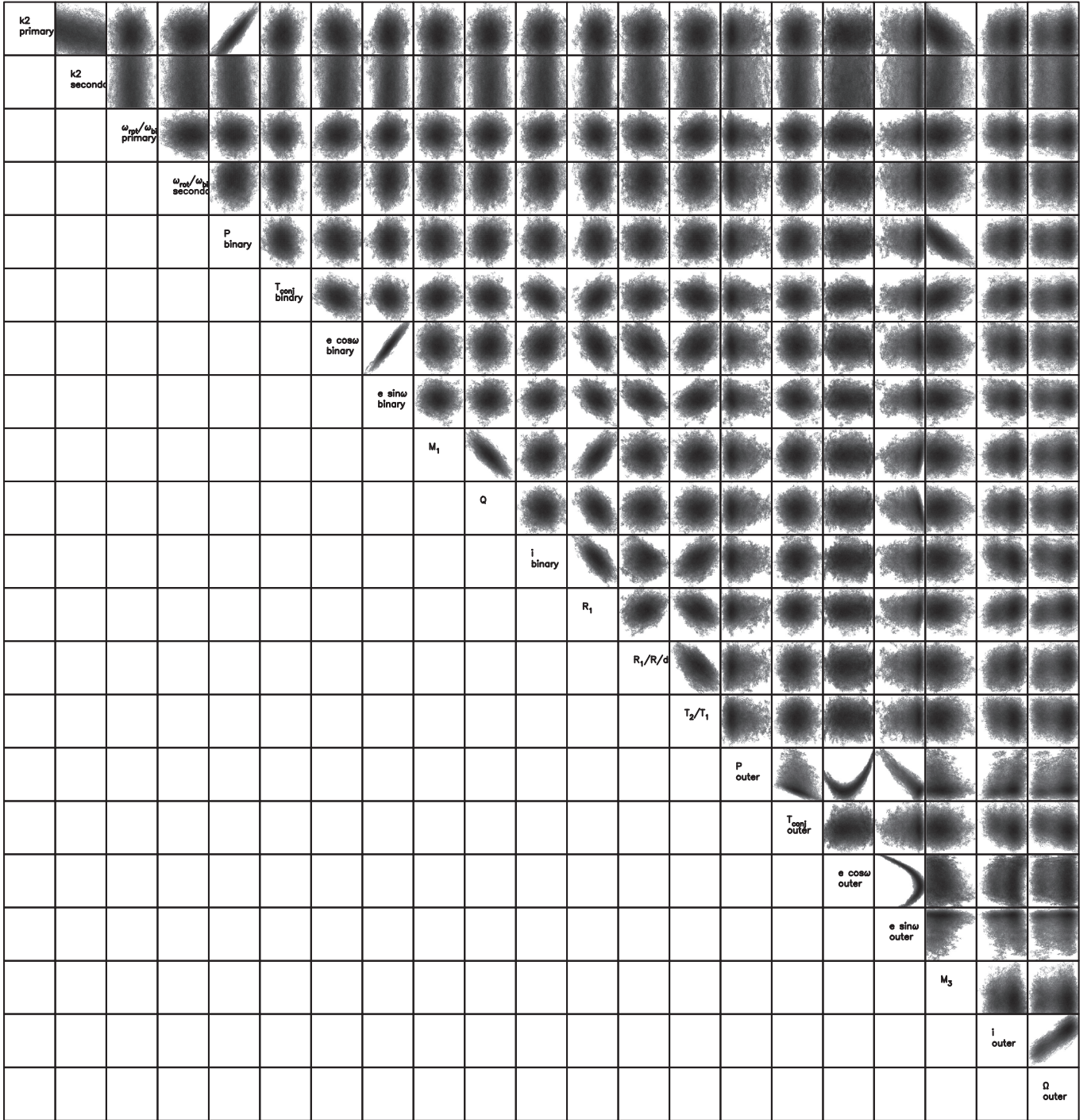
Figure 14. Correlations between the major parameters for the ELC photodynamical solution.

Claret (2006) within 1σ[44] (i.e., k_2(A, ELC) $= 0.003 \pm 0.005$ versus k_2(A, Claret, $M = 1.2\,M_\odot$) $= 0.004$), the nominal uncertainties on the secondary's constant indicate a tension (i.e., k_2(B, ELC) $= 0.03 \pm 0.0005$ versus k_2(B, Claret, $M = 1.0\,M_\odot$) $= 0.015$). To evaluate the significance of this tension on our results, we repeat the ELC fitting as described in the previous section, but fixing the apsidal constants to those from Claret (2006), i.e., k_2(A) $= 0.004$ and k_2(B) $= 0.015$.

The fixed-constants solution is well within 1σ of the solution presented in Tables 3 and 4 (where the constants are fit for), and the planet's mass remains virtually unchanged, i.e., M_p(best − fit, fixed k_2) $= 462 \pm 167\,M_{\rm Earth}$ versus M_p(best − fit, free k_2) $= 483 \pm 206\,M_{\rm Earth}$.

5.2. The CP

Prior to the discovery of Kepler-1647b, all the known *Kepler* CBPs were Saturn sized and smaller (the largest being Kepler-34b, with a radius of $0.76\,R_{\rm Jup}$) and were found to orbit their host binaries within a factor of two from their

---

[44] For 4.4 Gyr and $Z = 0.01$—closest to the derived age and metallicity of Kepler-1647.

Table 3
Fitting Parameters for the ELC Photodynamical Solution of the Kepler-1647 System

Parameter	Mode (with 68% Range)	Mean (with 68% Range)	Unit
Binary Star			
Orbital period, P_{bin}	$11.2588185^{+0.0000009}_{-0.0000007}$	$11.2588186^{+0.0000008}_{-0.0000007}$	days
Time of conjunction, T_{conj}	$-43.51995^{+0.00002}_{-0.000001}$	$-43.5199517^{+0.00001}_{-0.000001}$	BJD–2,455,000
$e_b \sin \omega_b$	$-0.1386^{+0.0008}_{-0.0005}$	$-0.1384^{+0.0007}_{-0.0007}$	⋯
$e_b \cos \omega_b$	$0.081418^{+0.000009}_{-0.000008}$	$0.081419^{+0.000008}_{-0.000009}$	⋯
Inclination, i_{bin}	$87.9305^{+0.0143}_{-0.0185}$	$87.9271^{+0.0176}_{-0.0151}$	°
Mass ratio, $Q = M_B/M_A$	$0.7943^{+0.0016}_{-0.0023}$	$0.7939^{+0.0019}_{-0.0019}$	⋯
Velocity semiamplitude, K_A	$55.2159^{+0.0544}_{-0.0665}$	$55.2091^{+0.0611}_{-0.0597}$	km s^{-1}
Fractional radius, R_A/R_B	$1.8562^{+0.0038}_{-0.0071}$	$1.8545^{+0.0055}_{-0.0054}$	⋯
Temperature ratio, T_B/T_A	$0.9360^{+0.0026}_{-0.0019}$	$0.9363^{+0.0024}_{-0.0022}$	⋯
Limb-darkening primary *Kepler*, $x1_I$	$0.9825^{+0.015}_{-0.49}$	$0.6641^{+0.3333}_{-0.1717}$	⋯
Limb-darkening primary *Kepler*, $x1_J$	$0.3975^{+0.2050}_{-0.14}$	$0.4968^{+0.1057}_{-0.2393}$	⋯
Limb-darkening secondary *Kepler*, $x1_U$	$0.2708^{+0.044}_{-0.0231}$	$0.2847^{+0.03}_{-0.0371}$	⋯
Limb-darkening secondary *Kepler*, $y1_U$	$0.361^{+0.06}_{-0.054}$	$0.3701^{+0.0509}_{-0.0631}$	⋯
Apsidal constant, $k_2(A)$	$0.0062^{+0.0023}_{-0.0030}$	$0.0058^{+0.0026}_{-0.0027}$	⋯
Apsidal constant, $k_2(B)$[a]:	0.0–0.03	⋯	⋯
Rotational-to-orbital frequency ratio, primary	$1.0751^{+0.0324}_{-0.0324}$	$1.0759^{+0.0315}_{-0.0333}$	⋯
Rotational-to-orbital frequency ratio, secondary	$1.3509^{+0.17325}_{-0.2153}$	$1.3152^{+0.2089}_{-0.1796}$	⋯
CB Planet			
Orbital period, P_p	$1107.5946^{+0.0173}_{-0.0119}$	$1107.6056^{+0.0063}_{-0.0229}$	days
Time of conjunction, T_{conj}[b]	$-1.5005^{+0.0058}_{-0.0058}$	$-1.5005^{+0.0059}_{-0.0058}$	BJD–2,455,000
$e_p \sin \omega_p$	$0.02516^{+0.0025}_{-0.0057}$	$0.02063^{+0.0069}_{-0.0012}$	⋯
$e_p \cos \omega_p$	$-0.0006^{+0.1232}_{-0.0784}$	$0.0394^{+0.0832}_{-0.1184}$	⋯
Inclination, i_p	$90.0962^{+0.0026}_{-0.0036}$	$90.0945^{+0.00436}_{-0.0019}$	°
Nodal longitude, Ω_p	$-2.0991^{+0.2041}_{-0.3368}$	$-2.3341^{+0.4392}_{-0.1017}$	°
Mass of planet b, M_p	$312.5000^{+175.0000}_{-308.3333}$	$344.4662^{+143.0338}_{-340.2996}$	M_{Earth}
Seasonal Contamination			
Season 0	$0.0776^{+0.0063}_{-0.0057}$	$0.0779^{+0.0059}_{-0.0061}$	⋯
Season 1	$0.0670^{+0.0066}_{-0.0054}$	$0.0676^{+0.0060}_{-0.0060}$	⋯
Season 2	0.0798 ± 0.0024	⋯	⋯
Season 3	$0.0753^{+0.0060}_{-0.0060}$	$0.0751^{+0.0062}_{-0.0058}$	⋯

Note.
[a] Allowed range.
[b] Conjunction with barycenter.

corresponding boundary for dynamical stability. Interestingly, "'Jupiter-mass CBPs are likely to be less common because of their less stable evolution," suggest PN08, and "if present (Jupiter-mass CBPs) are likely to orbit at large distances from the central binary." Indeed—at the time of writing, with a radius of 1.06 ± 0.01 R_{Jup} (11.8739 ± 0.1377 R_{Earth}) and mass of 1.52 ± 0.65 M_{Jup} (483 ± 206 M_{Earth}),[45] Kepler-1647b is the first Jovian transiting CBP from *Kepler*, and the one with the longest orbital period ($P_p = 1107.6$ days). The size and the mass of the planet are consistent with theoretical predictions indicating that substellar-mass objects evolve toward the radius of Jupiter after ∼1 Gyr of evolution for a wide range of initial masses (∼0.5–10 M_{Jup}), and regardless of the initial conditions ('hot' or "cold" start) (Burrows et al. 2001; Spiegel & Burrows 2013). To date, Kepler-1647b is also one of the longest-period transiting planets, demonstrating yet again the discovery potential of continuous, long-duration observations such as those made by *Kepler*. The orbit of the planet is nearly

edge-on ($i_p = 90°0972 \pm 0°0035$), with a semimajor axis $a_p = 2.7205 \pm 0.0070$ AU and eccentricity of $e_p = 0.0581 \pm 0.0689$.

5.3. Orbital Stability and Long-term Dynamics

Using Equation (3) from Holman & Wiegert 1999 (also see Dvorak 1986; Dvorak et al. 1989), the boundary for orbital stability around Kepler-1647 is at $a_{crit} = 2.91$ a_{bin}. With a semimajor axis of 2.72 AU (21.3 a_{bin}), Kepler-1647b is well beyond this stability limit, indicating that the orbit of the planet is long-term stable. To confirm this, we also integrated the planet-binary system using the best-fit ELC parameters for a timescale of 100 Myr. The results are shown in Figure 17. As seen from the figure, the semimajor axis and eccentricity of the planet do not experience appreciable variations (that would inhibit the overall orbital stability of its orbit) over the course of the integration.

On a shorter timescale, our numerical integration indicates that the orbital planes of the binary and the planet undergo a 7040.87 yr, anticorrelated precession in the plane of the sky.

_____
[45] See also Table 4 for mean and mode.

Table 4
Photodynamically Derived Parameters for the Kepler-1647 System (Osculating at BJD = 2,455,000)

Parameter	Best Fit	Mode (with 68% Range)	Mean (with 68% Range)	Unit
Mass of star A, M_A	1.2207 ± 0.0112	$1.2167^{+0.0054}_{-0.0059}$	$1.2163^{+0.0059}_{-0.0054}$	$M_\odot$
Mass of star B, M_B	0.9678 ± 0.0039	$0.9652^{+0.0036}_{-0.0027}$	$0.9656^{+0.0031}_{-0.0031}$	$M_\odot$
Mass of planet b, M_p[a]	483 ± 206	$312.5000^{+175.0000}_{-308.3333}$	$344.4662^{+143.0338}_{-340.2996}$	M_{Earth}
Radius of star A, R_A	1.7903 ± 0.0055	$1.7871^{+0.0026}_{-0.0043}$	$1.7873^{+0.0034}_{-0.00352}$	$R_\odot$
Radius of star B, R_B	0.9663 ± 0.0057	$0.9636^{+0.0032}_{-0.0030}$	$0.9637^{+0.0030}_{-0.0031}$	$R_\odot$
Radius of planet, R_p	11.8739 ± 0.1377	$11.8504^{+0.0677}_{-0.0804}$	$11.8438^{+0.0743}_{-0.0738}$	R_{Earth}
Gravity of star A, $\log g_A$	4.0180 ± 0.0020	$4.0181^{+0.0017}_{-0.0016}$	$4.0182^{+0.0016}_{-0.0017}$	cgs
Gravity of star B, $\log g_B$	4.4534 ± 0.0040	$4.4555^{+0.0018}_{-0.0032}$	$4.4544^{+0.0028}_{-0.0022}$	cgs
Binary Orbit				
Orbital period, P_{bin}[a]	11.2588179 ± 0.0000013	$11.2588185^{+0.0000009}_{-0.0000007}$	$11.2588186^{+0.0000008}_{-0.0000007}$	days
Time of conjunction, T_{conj}[a]	-43.51995 ± 0.00002	$-43.51995^{+0.0002}_{-0.000001}$	$-43.5199517^{+0.00001}_{-0.000001}$	BJD–2,455,000
Semimajor axis, a_{bin}	0.1276 ± 0.0002	$0.1275^{+0.0002}_{-0.0002}$	$0.12751^{+0.0002}_{-0.0002}$	AU
Eccentricity, e_{bin}	0.1602 ± 0.0004	$0.1607^{+0.0005}_{-0.0006}$	$0.1606^{+0.0006}_{-0.0006}$	...
Inclination, i_{bin}[a]	87.9164 ± 0.0145	$87.9305^{+0.0143}_{-0.0185}$	$87.9271^{+0.0176}_{-0.0151}$	°
Argument of periastron, ω_{bin}	300.5442 ± 0.0883	$300.4233^{+0.1600}_{-0.0867}$	$300.4621^{+0.1213}_{-0.1254}$	°
Apsidal precession, $\Delta\omega$ (ELC)[b]	0.0002420	...	...	°/cycle
Apsidal precession, $\Delta\omega$ (analytic), GR	0.0001873	...	...	°/cycle
Apsidal precession, $\Delta\omega$ (analytic), tidal	0.0000336	...	...	°/cycle
Planetary Orbit				
Orbital period, P_p[a]	1107.5923 ± 0.0227	$1107.5946^{+0.0173}_{-0.0119}$	$1107.6056^{+0.0063}_{-0.0229}$	days
Time of conjunction, T_{conj}[a]	-1.5028 ± 0.0049	$-1.5005^{+0.0058}_{-0.0058}$	$-1.5005^{+0.0059}_{-0.0058}$	BJD–2,455,000
Semimajor axis, a_p	2.7205 ± 0.0070	$2.7183^{+0.0032}_{-0.0040}$	$2.7177^{+0.0038}_{-0.0034}$	AU
Eccentricity, e_p	0.0581 ± 0.0689	$0.0275^{+0.08165}_{-0.0035}$	$0.0881^{+0.0210}_{-0.0641}$	...
Inclination, i_p[a]	90.0972 ± 0.0035	$90.0962^{+0.0026}_{-0.0036}$	$90.0945^{+0.00436}_{-0.0019}$	°
Argument of periastron, ω_p	155.0464 ± 146.5723	$4.250^{+161.5667}_{-4.933}$	$68.7878^{+97.0289}_{-69.4711}$	°
Nodal longitude, Ω_p[a]	-2.0393 ± 0.3643	$-2.0991^{+0.2041}_{-0.3368}$	$-2.3341^{+0.4392}_{-0.1017}$	°
Mutual orbital inclination, Δi[c]	2.9855 ± 0.2520	$3.019^{+0.238}_{-0.140}$	$3.194^{+0.062}_{-0.316}$	°

Notes. The best-fit column reproduces the light curve; the mode and mean columns represent the MCMC-optimized parameters.
[a] For easier interpretation, we repeat here the Mode and Mean for these parameters that are listed in Table 3 as well.
[b] $k_2(A) = 0.00249 \pm 0.00522$ and $k_2(B) = 0.02979 \pm 0.00053$.
[c] $\cos(\Delta i) = \sin(i_{bin})\sin(i_p)\cos(\Delta\Omega) + \cos(i_{bin})\cos(i_p)$.

Table 5
Best-fit, Barycentric Cartesian Coordinates for the Kepler-1647 System at BJD = 2,455,000

Parameter	Primary Star	Secondary Star	CB Planet
M [$M_\odot$]	1.22067659415220042	0.967766001496474848	$1.45159791061409129 \times 10^{-3}$
x [AU]	$-3.78722501644566112 \times 10^{-2}$	$4.78054676980426904 \times 10^{-2}$	$-2.39301668324773467 \times 10^{-2}$
y [AU]	$-1.59238464640225146 \times 10^{-3}$	$2.01398578685853605 \times 10^{-3}$	$-3.63758119907132233 \times 10^{-3}$
z [AU]	$-4.55884242496607597 \times 10^{-2}$	$5.35371764610109713 \times 10^{-2}$	2.64347531964575655
V_x [AU/day]	$1.97567794427114841 \times 10^{-2}$	$-2.48961816644120461 \times 10^{-2}$	$-1.58170933420904401 \times 10^{-2}$
V_y [AU/day]	$-8.53253808750116679 \times 10^{-4}$	$1.07539120444087718 \times 10^{-3}$	$5.64830825578074218 \times 10^{-4}$
V_z [AU/day]	$-2.34418182175292165 \times 10^{-2}$	$2.95694015193574272 \times 10^{-2}$	$-9.52503798501482327 \times 10^{-4}$

Note. The observer is looking along the $+z$-direction, and the sky is in the xy plane.

This is illustrated in Figure 18. As a result of this precession, the orbital inclinations of the binary and the planet oscillate by $\sim0°.0372$ and $\sim2°.9626$, respectively (see top and middle panels in Figure 18). The mutual inclination between the planet and the binary star oscillates by $\sim0°.0895$, and the planet's ascending node varies by $\sim2°.9665$ (see middle and bottom left panels in Figure 17).

Taking into account the radii of the binary stars and planet, we found that CBP transits are possible only if the planet's inclination varies between $89°.8137$ and $90°.1863$. This transit window is represented by the red horizontal lines in the middle panel of Figure 18. The planet can cross the disks of the two stars only when the inclination of its orbit lies between these two lines. To demonstrate this, in the bottom panel of Figure 18 we expand the vertical scale near $90°$ and also show the impact parameter b for the planet with respect to the primary (solid green symbols) and secondary (open blue symbols). Transits only formally occur when the impact parameter, relative to the sum of the stellar and planetary radii, is less than unity. We computed the impact parameter at the times of transit, as well

Table 6
Input Parameters (Osculating) for Kepler-1647 Needed for the *Photodynam* Code (Carter et al. 2011)

3	0.0				
0.02	1e-20				
0.00036121310659	0.00028637377462	0.00000042954554			
0.00832910409711	0.00449544901109	0.00050567865570			
0.75809801560924	0.16689760802955	0.0			
0.38919885445149	0.46863637334167	0.0			
0.14297457592624	0.02356800780666	0.0			
0.12763642607906	0.16022073112714	1.53443053940587	−1.03769914810282	0.0	1.581592306154
2.72058352472999	0.05807789749374	1.57249365140452	2.70607009751131	−0.03559283766606	−1.023387804660

Note. For details see description at https://github.com/dfm/photodynam.
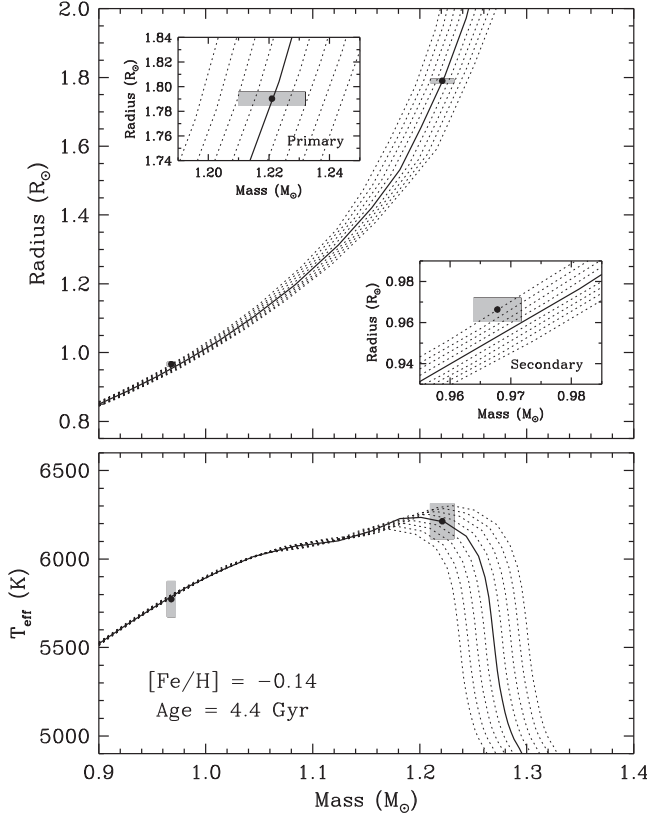
Figure 15. Radii (top) and temperatures (bottom) of the Kepler-1647 components as a function of mass, compared with stellar evolution models from the Yonsei-Yale series (Yi et al. 2001; Demarque et al. 2004). Model isochrones are shown for the best-fit metallicity of $[m/H] = -0.14$ and ages of 4.0–4.8 Gyr in steps of 0.1 Gyr, with the solid line marking the best-fit age of 4.4 Gyr. The insets in the top panel show enlargements around the primary and secondary observations.

Figure 16. Measurements for Kepler-1647 in the $\log g$–T_{eff} plane, along with 4.4 Gyr evolutionary tracks from the Yonsei-Yale series calculated for the measured masses and a metallicity of $[m/H] = -0.14$. The shaded area around each track indicates the uncertainty in its location stemming from the mass errors. The left track is for the primary star, the right track for the secondary star.

as at every conjunction, where a conjunction is deemed to have occurred if the projected separation of the planet and star is less than 5 planet radii along the *x*-coordinate.[46] Monitoring the impact parameter at conjunction allowed us to better determine the time span for which transits are possible, as shown in Figure 18. These transit windows, bound between the horizontal red lines in Figure 18, span about 204 yr each. As a result, over one precession cycle, planetary transits can occur for ≈408 yr (spanning two transit windows, half a precession cycle apart), i.e., ≈5.8% of the time. The transits of the CBP will cease in ~160 yr.

Following the methods described in Welsh et al. (2012), we used the probability of transit for Kepler-1647b to roughly estimate the frequency of Kepler-1647-like systems. At the present epoch, the transit probability is approximately 1/300 (i.e., $R_A/a_p \sim 0.33\%$), where the enhancement due to the barycentric motion of an aligned primary star is a minimal (~5%) effect. Folding in the probability of detecting two transits at two consecutive conjunctions of an 1100-day period planet when observing for 1400 days (i.e., 300/1400, or ~20%), the probability of detecting Kepler-1647b is therefore about 0.33% × 20%, or approximately 1/1500. Given that one such system was found out of *Kepler*'s ~150,000 targets, this suggests an occurrence rate of roughly 1%. A similar argument can be used to analyze the frequency among EBs in particular. As the population of EBs is already nearly aligned to the line of sight, the probability of alignment for the CBP is significantly increased. In particular, as described in Welsh et al. (2012), the probability that the planet will be aligned given that the target is an EB is approximately $a_{bin}/a_p = 0.046$ (compared to ~0.003 for the isotropic case). Recent results suggest that only EBs with periods longer than ~7 days contain CBPs (Welsh et al. 2014; Hamers et al. 2015; Martin et al. 2015; Muñoz & Lai 2015);
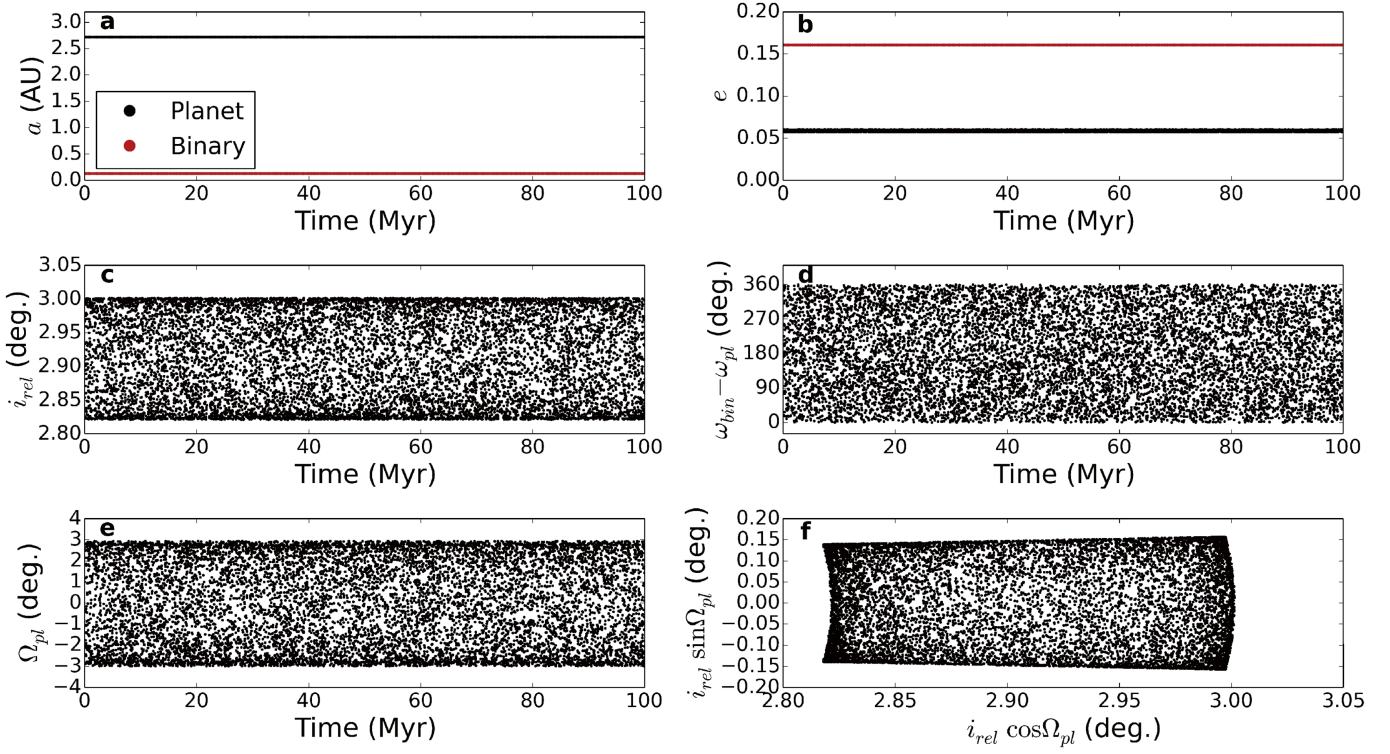
---

[46] The *xy*-coordinates define the plane of the sky, and the observer is along the *z*-coordinate.

Figure 17. Long-term (100 Myr) evolution of select orbital elements of the Kepler-1647 system. We do not observe chaotic behavior, confirming that the CBP is long-term stable.
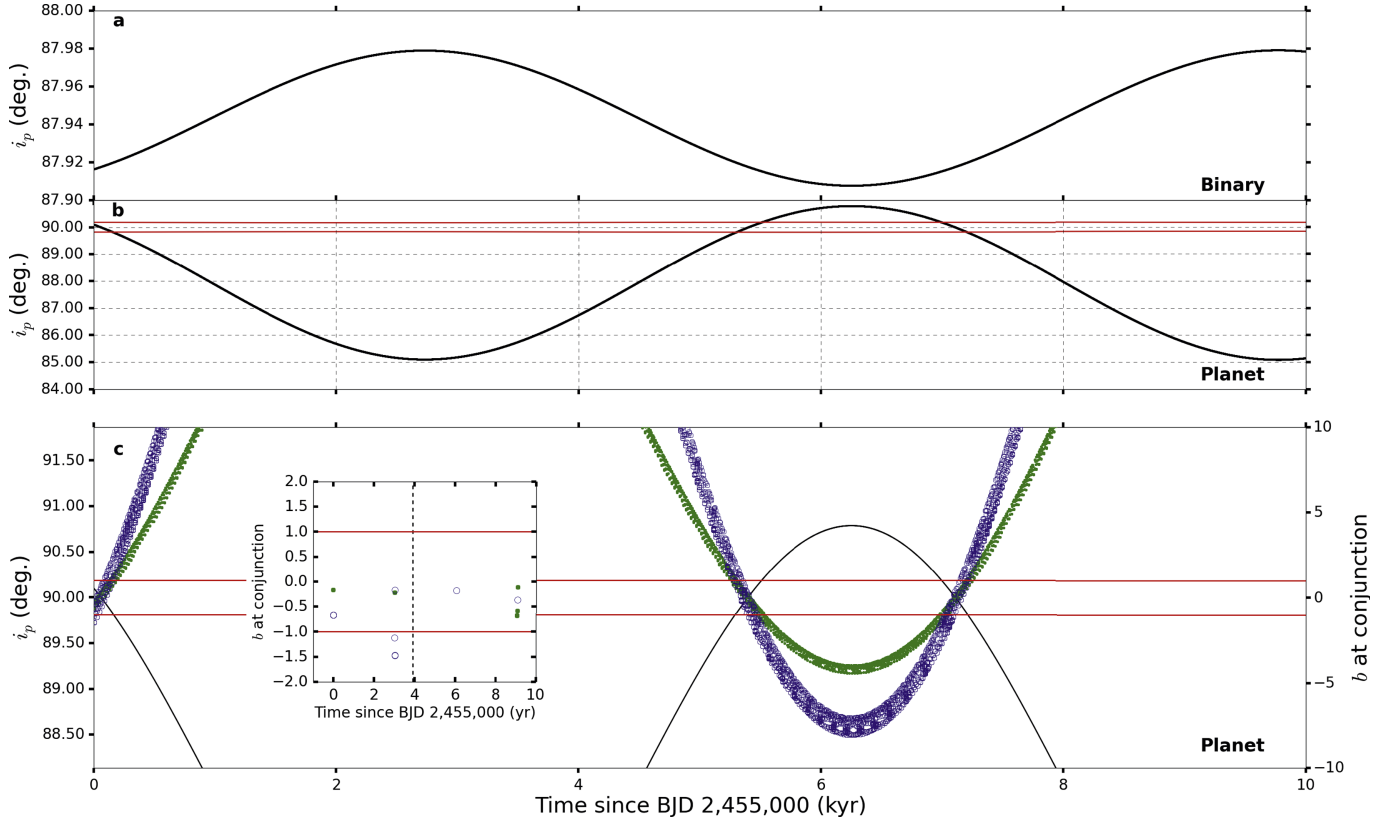

Figure 18. Precession of the orbital inclination (in the reference frame of the sky) of the binary star (top panel) and of the CBP (middle panel) over 10,000 yr, and evolution of the impact parameter (*b*) between the planet and each star (bottom panel). The solid, red horizontal lines in the middle panel represent the windows where planetary transits are possible. Each transit window is ≈204 yr, indicating that the CBP can transit for ≈5.8% of its precession cycle. The bottom panel is similar to the middle, but zoomed around the red horizontal band and showing the two impact parameters near primary (solid green symbols) and secondary (open blue symbols) conjunction. The inset in the bottom panel is zoomed around the duration of the *Kepler* mission, with the vertical dashed line indicating the last data point of Quarter 17. There were four transits over the duration of the mission, with one of them falling into a data gap (green symbol near time 0 in the inset panel).
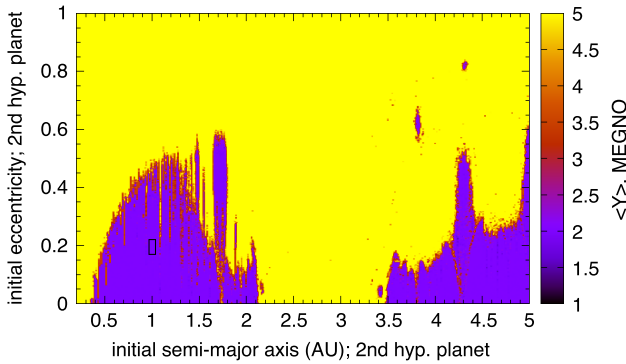
Figure 19. Dynamical stability (in terms of the MEGNO Y factor) for a hypothetical second planet, interior and coplanar to Kepler-1647b, and with the same mass, as a function of its orbital separation and eccentricity. The purple regions represent stable orbits for up to 2738 yr, indicating that there are plausible orbital configurations for such a planet. The MEGNO simulations reproduce well the critical dynamical stability limit at 0.37 AU. The square symbol represents the initial condition for a test orbit of a hypothetical second planet that we integrated for 10^7 yr, which we found to be stable.

Figure 20. Top view of the orbital configuration of the Kepler-1647 system at time BJD = 2,455,000. The figure shows the location of the HZ (green) and the planet's orbit (white circle). The binary star is in the center, surrounded by the critical limit for dynamical stability (red circle). The dark- and light-green regions represent the conservative and extended HZ, respectively (Kopparapu et al. 2013, 2014). The CBP is inside the conservative HZ for its entire orbit. The observer is looking from above the figure, along the direction of the arrow. A movie of the time evolution of the HZ can be found at http://astro.twam. info/hz-ptype.

there are ~1000 such *Kepler* EBs (Kirk et al. 2015). Thus, if 1% of these 1000 EBs have Kepler-1647-like CBPs, then the expected number of detections would be $0.02 \times 1000 \times 0.046 = 0.92 \approx 1$. As a result, the Kepler-1647 system suggests that ~2% of all eligible EBs have similar planets.

Cumming et al. (2008) suggest a ~1% occurrence rate of Jupiter-mass planets within the 2–3 AU range. Therefore, the relative frequency of such planets around FGK main-sequence stars is similar for both single and binary stars. This interesting result is consistent with what has been found for other CBPs as well and certainly has implications for planet formation theories. A more detailed analysis following the methods of Armstrong et al. (2014) and Martin & Triaud (2014) in the context of the full CBP population is beyond the scope of the present work.

We performed a thorough visual inspection of the light curve for additional transits. Our search did not reveal any obvious features.[47] However, given than Kepler-1647b is far from the limit for orbital stability, we also explored whether a hypothetical second planet, interior to Kepler-1647b, could have a stable orbit in the Kepler-1647 system, using the Mean Exponential Growth factor of Nearby Orbits (MEGNO) formalism (Goździewski et al. 2001; Cincotta et al. 2003; Hinse et al. 2015). Figure 19 shows the results of our simulations in terms of a two-planet MEGNO map of the Kepler-1647 system. The map has a resolution of $Nx = 500$ and $Ny = 400$ and was produced from a set of 20,000 initial conditions. The x and y axes of the figure represent the semimajor axis and eccentricity of the hypothetical second planet, respectively (with the same mass as Kepler-1647b). Each initial condition is integrated for 2738 yr, corresponding to 88,820 binary periods. A given run is terminated when the MEGNO factor Y becomes larger than 12. The map in Figure 19 shows the MEGNO factor in the interval $1 < Y < 5$. Quasi-periodic orbits at the end of the integration have $|\langle Y \rangle - 2.0| < 0.001$. The orbital elements used for creating this map are Jacobian geometric elements, where the semimajor axis of the planet is relative to the binary center of mass. All interactions (including planet–planet perturbation) are
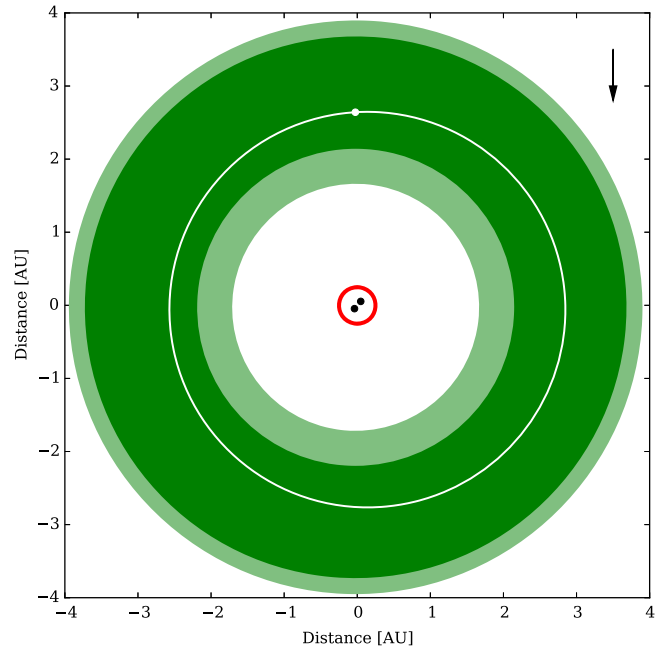
accounted for, and the orbits of the planets are integrated relative to the binary orbital plane. The initial mean anomaly of the second hypothetical planet is set to be 180° away from that of Kepler-1647b (i.e., the second planet starts at opposition). Quasi-periodic initial conditions are color-coded in purple in Figure 19, and chaotic dynamics is color-coded in yellow. As seen from the figure, there are regions where such a second planet may be able to maintain a stable orbit for the duration of the integrations. We further explored our MEGNO results by integrating a test orbit of the hypothetical second planet for 10^7 yr,[48] and we found it to be stable (for the duration of the integrations) with no significant onset of chaos. However, we note that the orbital stability of such a hypothetical planet will change dramatically depending on its mass.

5.4. Stellar Insolation and Circumbinary Habitable Zone

Using the formalism presented by Haghighipour & Kaltenegger (2013), we calculated the circumbinary habitable zone (HZ) around Kepler-1647. Figure 20 shows the top view of the HZ and the orbital configuration of the system at the time of the orbital elements in Table 4. The boundary for orbital stability is shown in red, and the orbit of the planet is in white. The light and dark green regions represent the extended and conservative HZs (Kopparapu et al. 2013, 2014), respectively. The arrow shows the direction from the observer to the system. As shown here, although it takes 3 yr for Kepler-1647b to complete one orbit around its host binary star, our best-fit model places this planet squarely in the conservative HZ for the entire duration of

---

[47] A single feature reminiscent of a very shallow transit-like event can be seen near day 1062 (BJD–2,455,000), but we could not associate it with the planet.

[48] Using an accurate adaptive-time step algorithm, http://www.unige.ch/ ~hairer/prog/nonstiff/odex.f.
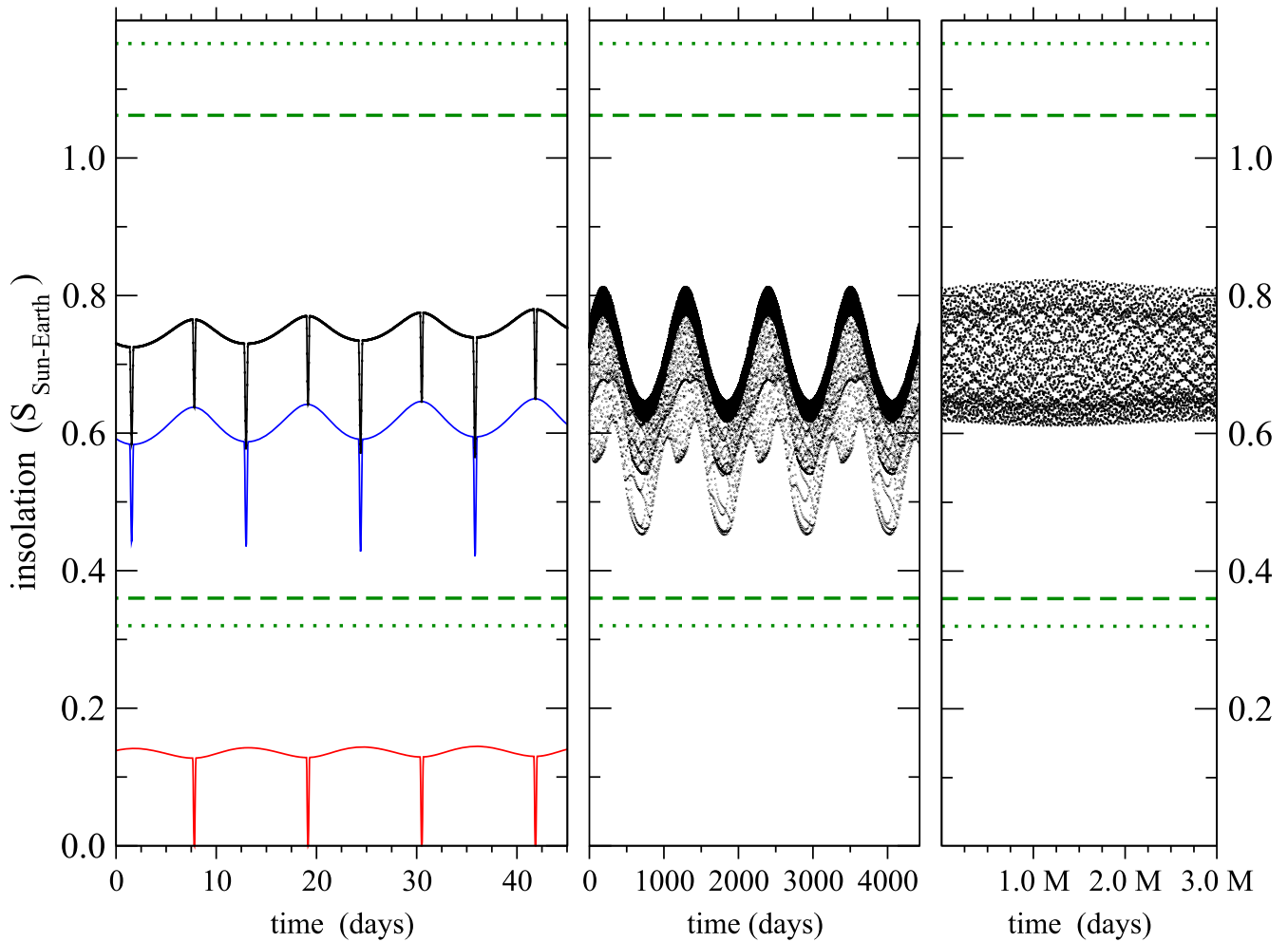
Figure 21. Time evolution of the stellar flux (black curve) reaching the top of the CBP's atmosphere. The blue and red curves in the left panel represent the flux from the primary and secondary star, respectively. The three panels represent the flux received by the CBP over four binary periods (left), four planetary periods (middle), and 3,000,000 days (right panel, with a sampling of every 500 days). The sharp features in the left panel represent the stellar eclipses (as seen from the planet); these are not present in the right panel due to the time sampling of the panel. The green dashed/dotted lines represent, from top to bottom, the runaway greenhouse, recent Venus, maximum greenhouse, and early Mars limits from Kopparapu et al. (2013, 2014). The CBP is inside the conservative HZ for its entire orbit.

its orbit. This makes Kepler-1647b the fourth of 10 currently known transiting CBPs that are in the HZ of their host binary stars.

Figure 21 shows the combined and individual stellar fluxes reaching the top of the planet's atmosphere. The sharp drops in the left and middle panels of the figure are due to the stellar eclipses as seen from the planet; these are not visible in the right panel due to the panel's sampling (500 days). The time-averaged insolation experienced by the CBP is $0.71 \pm 0.06\ S_{Sun-Earth}$. We caution that showing the summation of the two fluxes, as shown in this figure, is merely for illustrative purposes. This summation cannot be used to calculate the boundaries of the HZ of the binary star system. Because the planet's atmosphere is the medium through which insolation is converted to surface temperature, the chemical composition of this atmosphere plays an important role. As a result, the response of the planet's atmosphere to the stellar flux received at the location of the planet strongly depends on the wavelengths of incident photons, which themselves vary with the spectral type of the two stars. This means that in order to properly account for the interaction of an incoming photon with the atmosphere of the planet, its contribution has to be weighted based on the spectral type (i.e., the surface temperature) of its emitting star. It is the sum of the spectrally weighted fluxes of the

two stars of the binary that has to be used to determine the total insolation and therefore the boundaries of the system's HZ (Haghighipour & Kaltenegger 2013). The green dashed and dotted lines in Figure 21 show the upper and lower values of this weighted insolation. As shown in Figure 21, the insolation received at the location of the CBP's orbit is such that the planet is completely in its host binary's HZ.

For completeness, we note that while the gas giant Kepler-1647b itself is not habitable, it can potentially harbor terrestrial moons suitable for life as we know it (e.g., Forgan & Kipping 2013; Hinkel & Kane 2013; Heller 2014). There is, however, no evidence for such moons in the available data. Transit timing offsets due to even Gallilean-type moons would be less than 10 s for this planet.

6. CONCLUSIONS

We report the discovery and characterization of Kepler-1647b—a new transiting CBP from the *Kepler* space telescope. In contrast to the previous transiting CBPs, where the planets orbit their host binaries within a factor of two of their respective dynamical stability limit, Kepler-1647b is comfortably separated from this limit by a factor of 7. The planet has

Table 7
Kepler-1647: the Eclipsing Binary

Parameter	Value	Uncertainty (1σ)	Unit	Notes
Orbital period, P_{bin}	11.25882	0.00060	days	Pr\u0161a et al. (2011)
Epoch of periastron passage, T_0	−47.86903	0.00267	days[a]	Spectroscopy
Velocity semiamplitude, K_A	55.73	0.21	km s^{-1}	Spectroscopy
Velocity semiamplitude, K_B	69.13	0.50	km s^{-1}	Spectroscopy
System velocity offset, γ	18.00	0.13	km s^{-1}	Spectroscopy
Eccentricity, e_{bin}	0.1593	0.0030	...	Spectroscopy
Argument of periapsis, ω_{bin}	300.85	0.91	°	Spectroscopy
Semimajor axis, $a_A \sin i$	12.24	0.04	$R_\odot$	Spectroscopy
Semimajor axis, $a_B \sin i$	15.19	0.11	$R_\odot$	Spectroscopy
Semimajor axis, $a_{bin} \sin i$	27.43	0.12	$R_\odot$	Spectroscopy
Mass of star A, $M_A \sin^3 i$	1.210	0.019	$M_\odot$	Spectroscopy
Mass of star B, $M_B \sin^3 i$	0.975	0.010	$M_\odot$	Spectroscopy
Mass ratio, $Q = M_B/M_A$	0.8062	0.0063	...	Spectroscopy
Temperature of star A, T_A	6210	100	K	Spectroscopy
Temperature of star B, T_B	5770	125	K	Spectroscopy
Flux ratio, F_B/F_A	0.21	0.02	...	Spectroscopy
$V \sin i$ of star A, $V \sin i$	8.4	0.5	km s^{-1}	Spectroscopy
$V \sin i$ of star B, $V \sin i$	5.1	1.0	km s^{-1}	Spectroscopy
Fe/H of star A, [Fe/H]	−0.14	0.05	...	Spectroscopy
Age	4.4	0.25	Gyr	Spectroscopy
Normalized semimajor axis, R_A/a_{bin}	0.0655	0.0002	...	Photometry[b]
Normalized semimajor axis, R_B/a_{bin}	0.0354	0.0001	...	Photometry
Flux ratio, F_B/F_A	0.22	0.02	...	Photometry
Flux contamination $F_{cont, imaging}$	0.069	0.015	...	Photometry
Flux contamination (mean), $F_{cont,MAST}$	0.04	0.01	...	MAST

Notes.
[a] BJD–2,455,000.
[b] Based on pre-photodynamic analysis of the *Kepler* data.

an orbital period of ∼1100 days and a radius of 1.06 ± 0.01 R_{Jup}. At the time of writing, Kepler-1647b is the longest-period, largest transiting CBP, and it is also one of the longest-period transiting planets. With 1.52 ± 0.65 M_{Jup}, this CBP is massive enough to measurably perturb the times of the stellar eclipses. Kepler-1647b completed a single revolution during *Kepler*'s observations and transited three times, one of them as a syzygy. We note that the next group of four transits (starting around date BJD = 2,458,314.5, or UT of 2018 July 15; see Table 2) will fall within the operation time frame of *TESS*. The orbit of this CBP is long-term stable, with a precession period of ∼7040 yr. Due to its orbital configuration, Kepler-1647b can produce transits for only ≈5.8% of its precession cycle. Despite having an orbital period of 3 yr, this planet is squarely in the conservative HZ of its binary star for the entire length of its orbit.

The stellar system consists of two stars with $M_A = 1.2207 \pm 0.0112\,M_\odot$, $R_A = 1.7903 \pm 0.0055\,R_\odot$ and $M_B = 0.9678 \pm 0.0039\,M_\odot$, $R_B = 0.9663 \pm 0.0057\,R_\odot$ on a nearly edge-on orbit with an eccentricity of 0.1602 ± 0.0004. The two stars have a flux ratio of $F_B/F_A = 0.21 \pm 0.02$, the secondary is an active star with a rotation period of $P_{rot} = 11.23 \pm 0.01$ days, and the binary is in a spin-synchronized state. The two stars have effective temperatures of $T_{A,eff} = 6210 \pm 100$ K and $T_{B,eff} = 5770 \pm 125$ K, respectively, metallicity of [Fe/H] = -0.14 ± 0.05, and age of 4.4 ± 0.25 Gyr.

As important as a new discovery of a CBP is to indulge our basic human curiosity about distant worlds, its main significance is to expand our understanding of the inner workings of planetary systems in the dynamically rich environments of close binary stars. The orbital parameters of CBPs, for example, provide important new insight into the properties of protoplanetary disks and shed light on planetary formation and migration in the dynamically challenging environments of binary stars. In particular, the observed orbit of Kepler-1647b lends strong support to the models suggesting that CBPs form at large distances from their host binaries and subsequently migrate as a result of either planet–disk interaction or planet–planet scattering (e.g., Pierens & Nelson 2013; Kley & Haghighipou 2014, 2015).

REFERENCES

Akeson, R. L., Chen, X., Ciardi, D., et al. 2013, PASP, 125, 989
Armstrong, D. J., Osborn, H. P., Brown, D. J. A., et al. 2014, MNRAS, 444, 1873
Bastien, F., Stassun, K. G., & Pepper, J. 2014, ApJ, 788, 9
Borucki, W. J., & Summers, A. L. 1984, Icar, 58, 121
Boyajian, T. S., von Braun, K., van Belle, G., et al. 2012, ApJ, 757, 112
Bromley, B. C., & Kenyon, S. J. 2015, ApJ, 806, 98
Brown, T. M., Latham, D. W., Everett, M. E., et al. 2011, AJ, 142, 112
Bryson, S. T., Jenkins, J. M., Gilliland, R. L., et al. 2013, PASP, 125, 889
Buchhave, L. A., Bakos, G. A., Hartman, J. D., et al. 2010, ApJ, 720, 1118
Burrows, A., Hubbard, W. B., Lunine, J. I., et al. 2001, RvMP, 73, 719
Carter, J. A., Fabrycky, D., Ragozzine, D., et al. 2011, Sci, 331, 562
Chavez, C. E., Georgakarakos, N., Prodan, S., et al. 2015, MNRAS, 446, 1283
Cincotta, P. M., Giordano, C. M., & Simó, C. 2003, PhyD, 182, 151
Claret, A. 2006, A&A, 453, 769
Clausen, J. V., Bruntt, H., Claret, A., et al. 2009, A&A, 502, 253
Conroy, K., Prsa, A., Stassun, K. G., et al. 2014, AJ, 147, 45
Cumming, A., Butler, R. P., Marcy, G. W., et al. 2008, PASP, 120, 531
Deck, K., & Agol, E. 2015, ApJ, 802, 116
Deeg, H.-J., Doyle, L. R., Kozhevnikov, V. P., et al. 1998, A&A, 338, 479
Demarque, P., Woo, J.-H., Kim, Y.-C., & Yi, S. K. 2004, ApJS, 155, 667
Doyle, A. P., Davies, G. R., Smalley, B., et al. 2014, MNRAS, 444, 3592
Doyle, L. R., Carter, J. A., Fabrycky, D. C., et al. 2011, Sci, 333, 6049
Doyle, L. R., & Deeg, H.-J. 2004, in IAU Symp. 213, Bioastronomy 2002: Life among the Stars, ed. R. P. Norris & F. H. Stootman (San Francisco, CA: ASP), 80
Doyle, L. R., Deeg, H.-J., & Kozhevnikov, V. P. 2000, ApJ, 535, 338
Dressing, C. D., Adams, E. R., Dupree, A. K., Kulesa, C., & McCarthy, D. 2014, AJ, 148, 78
Dvorak, R. 1986, A&A, 167, 379
Dvorak, R., Froeschle, C., & Froeschle, Ch. 1989, A&A, 226, 335
Eastman, J., Silverd, R., & Gaudi, S. B. 2010, PASP, 122, 935
Fabrycky, D. C., & Tremaine, S. 2007, ApJ, 669, 1289
Feroz, F., Hobson, M. P., & Bridges, M. 2008, MNRAS, 384, 449
Forgan, D., & Kipping, D. 2013, MNRAS, 432, 2994
Foucart, F., & Lai, D. 2013, ApJ, 764, 106
Foucart, F., & Lai, D. 2014, MNRAS, 445, 1731
Füresz, G. 2008, PhD thesis, Univ. Szeged
Gilliland, R. L., Chaplin, W. J., Dunham, E. W., et al. 2011, ApJS, 197, 6
Goździewski, K., Bois, E., Maciejewski, A. J., & Kiseleva-Eggleton, L. 2001, A&A, 378, 569
Gray, D. F. 1984, ApJ, 281, 719
Greiss, S., Steeghs, D., Gansicke, B. T., et al. 2012, AJ, 144, 24
Haghighipour, N., & Kaltenegger, L. 2013, ApJ, 777, 166

Hairer, E., Lubich, C., & Wanner, G. 2003, AN, 12, 399
Hamers, A., Perets, H. B., & Portegies Zwart, S. 2015, arXiv:1506.02039
Heller, R. 2014, ApJ, 787, 14
Hilditch, R. W. (ed.) 2001, An Introduction to Close Binary Stars (Cambridge: Cambridge Univ. Press), 392
Hinkel, N. R., & Kane, S. 2013, ApJ, 774, 27
Hinse, T. C., Haghighipour, N., Kostov, V. B., & Goździewski, K. 2010, ApJ, 799, 88
Hinse, T. C., Lee, J. W., Goździewski, K., et al. 2014, MNRAS, 438, 307
Hinse, T. C., Haghighipour, N., Kostov, V. B., & Gozdziewski, K. 2015, ApJ, 799, 88
Holczer, T., Shporer, A., Mazeh, T., et al. 2015, ApJ, 870, 170
Holman, M. J., & Wiegert, P. A. 1999, AJ, 117, 621
Horner, J., Hinse, T. C., Wittenmyer, R. A., et al. 2012, MNRAS, 427, 2812
Horner, J., Marshall, J. P., Wittenmyer, R. A., & Tinney, C. G. 2011, MNRAS, 416, 11
Howell, S. B., Rowe, J. F., Bryson, S. T., et al. 2012, ApJ, 746, 123
Hut, P. 1981a, A&A, 99, 126
Hut, P. 1981b, BAAS, 14, 902
Hut, P. 1982, A&A, 110, 37
Jenkins, J. M., Doyle, L. R., & Cullers, K. 1996, Icar, 119, 244
Kirk, B., Conroy, K., Prsa, A., et al. 2016, AJ, 151, 68
Kipping, D. M. 2013, MNRAS, 435, 2152
Kley, W., & Haghighipou, N. 2014, A&A, 564, 72
Kley, W., & Haghighipou, N. 2015, A&A, 581, 20
Koch, D. G., Borucki, W. J., Basri, G., et al. 2010, ApJ, 713, 79
Kolbl, R., Marcy, G. W., Isaacson, H., & Howard, A. W. 2015, AJ, 149, 18
Kopparapu, R. K., Ramirez, R., Kasting, J. F., et al. 2013, ApJ, 765, 2
Kopparapu, R. K., Ramirez, R. M., James, S., et al. 2014, ApJ, 787, 29
Kostov, V. B., McCullough, P. R., Carter, J. A., et al. 2014, ApJ, 784, 14
Kostov, V. B., McCullough, P. R., Hinse, T. C., et al. 2013, ApJ, 770, 52
Kovács, G., Zucker, S., & Mazeh, T. 2002, A&A, 391, 369
Kozai, Y. 1962, AJ, 67, 591
Latham, D. W., Stefanik, R. P., Torres, G., et al. 2002, AJ, 124, 1144
Lawrence, A., Warren, S. J., Almaini, O., et al. 2007, MNRAS, 379, 1599
Lidov, M. L. 1962, P&SS, 9, 719
Lines, S., Leinhardt, Z. M., Baruteau, C., et al. 2015, A&A, 582, 5
Mandel, K., & Agol, E. 2002, ApJL, 580, L171
Mardling, R. A., & Lin, D. N. C. 2002, ApJ, 573, 829
Martin, D. V., Mazeh, T., & Fabrycky, D. C. 2015, MNRAS, 453, 3554
Martin, D. V., & Triaud, A. H. M. J. 2014, A&A, 570, 91
Martin, D. V., & Triaud, A. H. M. J. 2015, MNRAS, 449, 781
Marzari, F., Thebault, P., Scholl, H., et al. 2013, A&A, 553, 71
Matijevic, G., Prsa, A., Orosz, J. A., et al. 2012, AJ, 143, 123
Mazeh, T., Holczer, T., & Shporer, A. 2015, ApJ, 800, 142
Mazeh, T., & Shaham, J. 1979, A&A, 77, 145
McQuillan, A., Aigrain, S., & Mazeh, T. 2013a, MNRAS, 432, 1203
McQuillan, A., Mazeh, T., & Aigrain, S. 2013b, ApJ, 775, 11
McQuillan, A., Mazeh, T., & Aigrain, S. 2014, ApJS, 211, 24
Meibom, S., Barnes, S. A., Latham, D., et al. 2011, ApJ, 733, 9
Meixner, M., Smee, S., Doering, R. L., et al. 2010, PASP, 122, 890
Meschiari, S. 2013, arXiv:1309.4679
Miranda, R., & Lai, D. 2015, MNRAS, 452, 2396
Munoz, D., & Lai, D. 2015, PNAS, 112, 9264
Murray, C. D., & Correia, A. C. M. 2011, in Exoplanets, ed. S. Seager (Tucson, AZ: Univ. Arizona Press)
Nordstroem, B., Latham, D. W., Morse, J. A., et al. 1994, A&A, 287, 338
Orosz, J. A., & Hauschildt, P. H. 2000, A&A, 364, 265
Orosz, J. A., Welsh, W. F., Carter, J. A., et al. 2012a, ApJ, 758, 87
Orosz, J. A., Welsh, W. F., Carter, J. A., et al. 2012b, Sci, 337, 1511
Paardekooper, S.-J., Leinhardt, Z. M., Thbault, P., & Baruteau, C. 2012, ApJ, 754, 16
Pál, A. 2012, MNRAS, 420, 1630
Pelupessy, F. I., & Portegies Zwart, S. 2013, MNRAS, 429, 895
Pepper, J., Pogge, R., DePoy, D. L., et al. 2007, PASP, 119, 923
Pierens, A., & Nelson, R. P. 2007, A&A, 472, 993
Pierens, A., & Nelson, R. P. 2008, A&A, 483, 633
Pierens, A., & Nelson, R. P. 2008a, A&A, 483, 633
Pierens, A., & Nelson, R. P. 2008b, A&A, 482, 333
Pierens, A., & Nelson, R. P. 2008c, A&A, 478, 939
Pierens, A., & Nelson, R. P. 2013, A&A, 556, 134
Prša, A., Batalha, N., Slawson, R. W., et al. 2011, AJ, 141, 83
Rafikov, R. 2013, ApJ, 764, 16
Raghavan, D., McAlister, H. A., Henry, T. J., et al. 2010, ApJS, 191, 1

Schleicher, D. R. G., Dreizler, S., Völschow, M., Banerjee, R., & Hessman, F. V. 2015, AN, 336, 458
Schneider, J. 1994, P&SS, 42, 539
Schneider, J., & Chevreton, M. 1990, A&A, 232, 251
Schneider, J., & Doyle, L. R. 1995, EM&P, 71, 153
Schwamb, M. E., Orosz, J. A., Carter, J. A., et al. 2013, ApJ, 768, 127
Silsbee, K., & Rafikov, R. R. 2015, ApJ, 798, 71
Siverd, R. J., Beatty, T., Pepper, J., et al. 2012, ApJ, 761, 123
Skilling, J. 2004, in AIP Conf. Ser., Nested Sampling, ed. R. Fischer, R. Preuss, & U. V. Toussaint (Melville, NY: AIP) 395
Slawson, R. W., Prša, A., Welsh, W. F., et al. 2011, AJ, 142, 160
Spiegel, D. S., & Burrows, A. 2013, ApJ, 772, 76
ter Braak, C. J. F., & Vrugt, J. A. 2006, Statistics and Computing, 16, 239
Tal-Or, L., Mazeh, T., Alonso, R., et al. 2013, A&A, 553, 30
Tohline, J. E. 2002, ARA&A, 40, 349
Torres, G. 2013, AN, 334, 4
Torres, G., Andersen, J., & Giménez, A. 2010, A&ARv, 18, 67

Torres, G., Lacy, C. H., Marschall, L. A., Sheets, H. A., & Mader, J. A. 2006, ApJ, 640, 1018
Torres, G., Vaz, L. P. R., & Sandberg Lacy, C. H. 2008, AJ, 136, 2158
Tull, R. G., MacQueen, P. J., Sneden, C., & Lambert, D. L. 1995, PASP, 10, 251
Vogt, S. S. 1987, PASP, 99, 1214
Vogt, S. S., Allen, S. L., Bigelow, B. C., et al. 1994, Proc. SPIE, 2198, 362
Vos, J., Clausen, J. V., Jørgensen, U. G., et al. 2012, A&A, 540, A64
Welsh, W. F., Orosz, J. A., Carter, J. A., & Fabrycky, D. C. 2014, in Proc. IAU Symp. 293, Formation, Detection, and Characterization of Extrasolar Habitable Planets, ed. N. Haghighipour et al., 125
Welsh, W. F., Orosz, J. A., Carter, J. A., et al. 2012, Natur, 481, 475
Welsh, W. F., Orosz, J. A., Short, D. R., et al. 2015, ApJ, 809, 26
Winn, J. N., & Holman, M. 2005, ApJ, 628, 159
Yi, S., Demarque, P., Kin, Y.-C., et al. 2001, ApJS, 136, 417
Zorotovic, M., & Schreiber, M. R. 2013, A&A, 549, 95
Zucker, S., & Mazeh, T. 1994, ApJ, 420, 806